



The Panchromatic Hubble Andromeda Treasury. XX. The Disk of M31 is Thick

Julianne J. Dalcanton^{1,2}, Eric F. Bell³, Yumi Choi⁴, Andrew E. Dolphin⁵, Morgan Fouesneau⁶, Léo Girardi⁷,David W. Hogg^{1,8}, Anil C. Seth⁹, and Benjamin F. Williams²¹ Center for Computational Astrophysics, Flatiron Institute, 162 Fifth Avenue, New York, NY 10010, USA; jdalcanton@flatironinstitute.org² Department of Astronomy, Box 351580, University of Washington, Seattle, WA 98195, USA³ Department of Astronomy, University of Michigan, 1085 S. University Avenue, Ann Arbor, MI 48109, USA⁴ Department of Astronomy, University of California Berkeley, Berkeley, CA 94720, USA⁵ Raytheon, 1151 E. Hermans Road, Tucson, AZ 85706, USA⁶ Max Planck Institute für Astronomie, Königstuhl 17, D-69117, Heidelberg, Germany⁷ Osservatorio Astronomico di Padova—INAF, Vicolo dell’Osservatorio 5, I-35122 Padova, Italy⁸ Center for Cosmology and Particle Physics, Department of Physics, New York University, 4 Washington Pl #424, New York, NY 10003 USA⁹ University of Utah, Salt Lake City, UT, USA

Received 2023 March 8; revised 2023 April 10; accepted 2023 April 11; published 2023 July 31

Abstract

We present a new approach to measuring the thickness of a partially face-on stellar disk, using dust geometry. In a moderately-inclined disk galaxy, the fraction of reddened stars is expected to be 50% everywhere, assuming that dust lies in a thin midplane. In a thickened disk, however, a wide range of radii project onto the line of sight. Assuming stellar density declines with radius, this geometrical projection leads to differences in the numbers of stars on the near and far sides of the thin dust layer. The fraction of reddened stars will thus differ from the 50% prediction, with a deviation that becomes larger for puffier disks. We map the fraction of reddened red giant branch (RGB) stars across M31, which shows prominent dust lanes on only one side of the major axis. The fraction of reddened stars varies systematically from 20% to 80%, which requires that these stars have an exponential scale height h_z that is 0.14 ± 0.015 times the exponential scale length ($h_r \approx 5.5$ kpc). M31’s RGB stars must therefore have $h_z = 770 \pm 80$ pc, which is far thicker than the Milky Way’s thin disk, but comparable to its thick disk. The lack of a significant thin disk in M31 is unexpected, but consistent with its interaction history and high disk velocity dispersion. We suggest that asymmetric reddening be used as a generic criterion for identifying “thick disk”-dominated systems, and discuss prospects for future 3D tomographic mapping of the gas and stars in M31.

Unified Astronomy Thesaurus concepts: [Interstellar dust extinction \(837\)](#); [Andromeda Galaxy \(39\)](#); [Interstellar reddening \(853\)](#); [Interstellar medium \(847\)](#); [Galaxy structure \(622\)](#); [Galaxy stellar disks \(1594\)](#); [Galaxy disks \(589\)](#); [Multi-color photometry \(1077\)](#); [Interstellar dust \(836\)](#)

1. Introduction

Historically, the Milky Way has set our understanding of the structure of galaxy disks. The classical picture of massive disks—a rapidly-rotating thin stellar disk, embedded in a less massive, thicker, slowly-rotating stellar disk, both surrounded by an even more diffuse stellar halo of fast-moving stars—all developed in response to studies of the structure and kinematics of Milky Way stars (see the review by Bland-Hawthorn & Gerhard 2016).

Over the years, evidence has accumulated that many of these same features are present in other massive galaxies. Thickened, rotating stellar envelopes appear to be common around edge-on galaxies (e.g., Dalcanton & Bernstein 2002; Yoachim & Dalcanton 2008; Comerón et al. 2011; Elmegreen et al. 2017), and more extended stellar halos have been revealed in many galaxies (e.g., Mouhcine et al. 2010; Greggio et al. 2014; Ibata et al. 2014; Rejkuba et al. 2014; Crnojević et al. 2016; Merritt et al. 2016; Trujillo & Fliri 2016; Harmsen et al. 2017; D’Souza & Bell 2018a; Beraldo e Silva et al. 2021; Wu et al. 2021; Gilbert et al. 2022), though whether they are better analogs of the Milky Way’s low-metallicity hot stellar halo or its tidal debris is often unclear.

Within the Milky Way, the thin+thick disk and halo ansatz has become necessarily more complex as better data have accumulated and have moved beyond star counts to include kinematics and metal abundances (see, for example, the reviews by Bland-Hawthorn & Gerhard (2016) and Helmi (2020); noting the added complexity introduced by the identification of the Gaia Enceladus “sausage”; e.g., Belokurov et al. 2018; Deason et al. 2018; Haywood et al. 2018; Helmi et al. 2018). However, the basic utility of the original picture has remained a useful framework outside of the bulge/bar-dominated inner regions, given that it broadly separates a galaxy into a “high specific angular momentum, low velocity dispersion” component, a “high specific angular momentum, moderate velocity dispersion” component, and a “high velocity dispersion, low net angular momentum”¹⁰ component. It is particularly hard to justify more nuanced decompositions of external galaxies where the data are not as rich, and it becomes impossible to decompose unresolved, low-density stellar populations by their detailed kinematics, photometry, and abundance patterns, and where all of the structural and kinematic features can only be seen in projection.

This latter limitation is especially vexing, particularly when attempting to separate thick and thin disk subcomponents. When a galaxy is seen edge-on, one can potentially decompose

 Original content from this work may be used under the terms of the [Creative Commons Attribution 4.0 licence](#). Any further distribution of this work must maintain attribution to the author(s) and the title of the work, journal citation and DOI.

¹⁰ Individual tidal streams that contribute to the halo may have high specific angular momenta, but having an extended, roughly spherical distribution suggests that the net specific angular momentum is not high.

the disk into two components, albeit with substantial uncertainties in inferring the thin disk structure due to dust. However, there is no way to measure the vertical kinematics of both components simultaneously. The opposite problem occurs when a galaxy is more face-on. At best, one might be able to detect the signature of a thick disk in the kinematics of individual stars, but one could not actually measure its height directly. In short, simultaneously measuring the structure and velocity dispersions of thin and thick disk components becomes essentially intractable outside the Milky Way.

In this paper, we take advantage of a novel probe of disk structure along the line of sight that breaks this degeneracy, allowing us to solve for the vertical structure in M31—a face-on but partially inclined galaxy. Using the dust mapping technique from Dalcanton et al. (2015), we measure the fraction of stars that lie behind M31’s layer of dusty interstellar medium (ISM). We then show how the amplitude and spatial variation in this “reddening fraction” can be used to constrain the inclination of M31 and the thickness of its stellar disk. We show that M31’s stellar disk must be much thicker than that of the Milky Way, and as such is consistent with M31’s complex halo structure (e.g., Ibata et al. 2014), high internal stellar velocity dispersion (e.g., Battacharya et al. 2019; Dorman et al. 2015), recent merger-driven burst of star formation (Bernard et al. 2015; Williams et al. 2015), and a weak planetary nebula metallicity gradient (e.g., Jacoby & Ciardullo 1999; Sanders et al. 2012; Bhattacharya et al. 2022; Kwitter et al. 2012; Balick et al. 2013, 2017), which is likely due in part to projection effects smoothing out an intrinsically steeper population gradient in the older stars.

Beyond the measurement of M31’s disk structure, we discuss further possibilities for using the fraction of reddened stars as a diagnostic of stellar and ISM geometry. The model calculations presented here are quite general, and point to using apparent asymmetries in the reddening across galaxies as a generic signpost of significantly thickened stellar disks, even when the sort of detailed analysis in Dalcanton et al. (2015) is not available. Given that the thickness of stellar disks has long been recognized as an indicator of past dynamical heating from interactions (e.g., going back to Toth & Ostriker 1992), a census of disk thickness that includes galaxies that are not fully edge-on would be illuminating. We also discuss the wealth of information that can be extracted from local departures from the smooth models presented here. Any warping of the gas or stars (globally, or with respect of one to the other) will lead to deviations from the expected reddening fraction (e.g., Choi et al. 2018; Yanchulova Merica-Jones et al. 2021), as would any significant offset of the dusty ISM from the stellar midplane, such as might be expected for infalling or accreted gas. These features turn maps of dust reddening fractions into powerful constraints on the 3D distribution of the dense ISM and of warps in both the gas and stars.

2. Measuring Disk Geometry Using Dust

When the dusty ISM is in a thin layer, it is reasonable to assume that most stars will lie either in front of or behind the dust, with only a small fraction of stars being embedded within. With this assumption, which is most likely to hold for older, vertically-heated stellar populations, roughly half of a galaxy’s stars will be behind the dusty gas when viewed face-on, provided that the disk is sufficiently undisturbed that the gas has settled into the midplane.

When the same galaxy is viewed inclined along the line of sight, however, the apparent fraction of reddened stars can deviate from the expected value of one-half, even though the disk+dust geometry has remained fixed. Unlike a face-on disk, a given line of sight through an inclined disk samples a range of galactic radii. Because the stellar surface density drops with radius, stars in the inner disk will be overrepresented along a given line of sight. If those inner disk stars are on the near side of the dust, then the fraction of reddened stars will fall below one-half along that particular line of sight. Conversely, if those inner disk stars are on the far side, then the apparent reddened fraction will be higher than one-half. This effect of geometry will therefore imprint a spatial pattern on a map of the fraction of reddened stars, depending on whether one is viewing the near or far side of the inclined disk. Elmegreen & Block (1999) have previously used this effect to explain why asymmetric patterns of dust reddening do not necessarily imply asymmetric distributions of the dust itself, and in M31 Merrett et al. (2006) have used this effect to explain spatial variations in the planetary nebula luminosity function.

The size of this effect depends strongly on position within the galaxy, and on the disk+dust geometry. The range of radii that a given line of sight samples (and thus the amplitude of the shift in the reddening fraction) will be larger when the disk is intrinsically thicker, or is more inclined along the line of sight. In addition, the effect will be negligible along the major axis, where lines of sight sample a range of azimuthal angles, but all at approximately the same radii for an undisturbed disk. The major axis will therefore always show a reddened fraction of 50% assuming it is aligned with the line of nodes.

The net result is that a map of the fraction of reddened stars is an excellent probe of disk structure and viewing geometry. The location of the 50% reddening line indicates the location of the major axis at each radius, and is therefore sensitive to the position angle and its radial variation. The rapidity with which the reddening fraction varies with distance from the major axis, and the amplitude of that variation, simultaneously constrains the inclination of the disk and its thickness compared to the radial scale length of the disk. As the radial scale length can be measured along the major axis itself, modeling the map of the reddening fraction provides a new way to measure the thickness of the stellar disk.

2.1. Calculating the Positional Dependence of f_{red}

We calculate the above effects by adopting a simple model where the stellar disk is radially exponential with a scale length h_r and has a vertical exponential distribution with scale height h_z . For this model, the space density of stars as a function of the radius r and height z above the midplane is

$$\rho(r, z) = \rho_0 e^{-r/h_r} e^{-|z|/h_z}, \quad (1)$$

where ρ_0 is the density in the very center of the galaxy. We calculate the surface density of stars that are in front of (Σ_+) or behind (Σ_-) the midplane by integrating the density ρ along the line of sight from the midplane, to positive or negative infinity, respectively. The total stellar surface density Σ will then be $\Sigma_+ + \Sigma_-$, which is equal to $\Sigma_0 = 2\rho_0 h_z$ in the center of the galaxy.

We perform the path integration along the variable l defined to be zero at the midplane. Along the integration path, for a galaxy with an inclination of i , the height above the midplane is

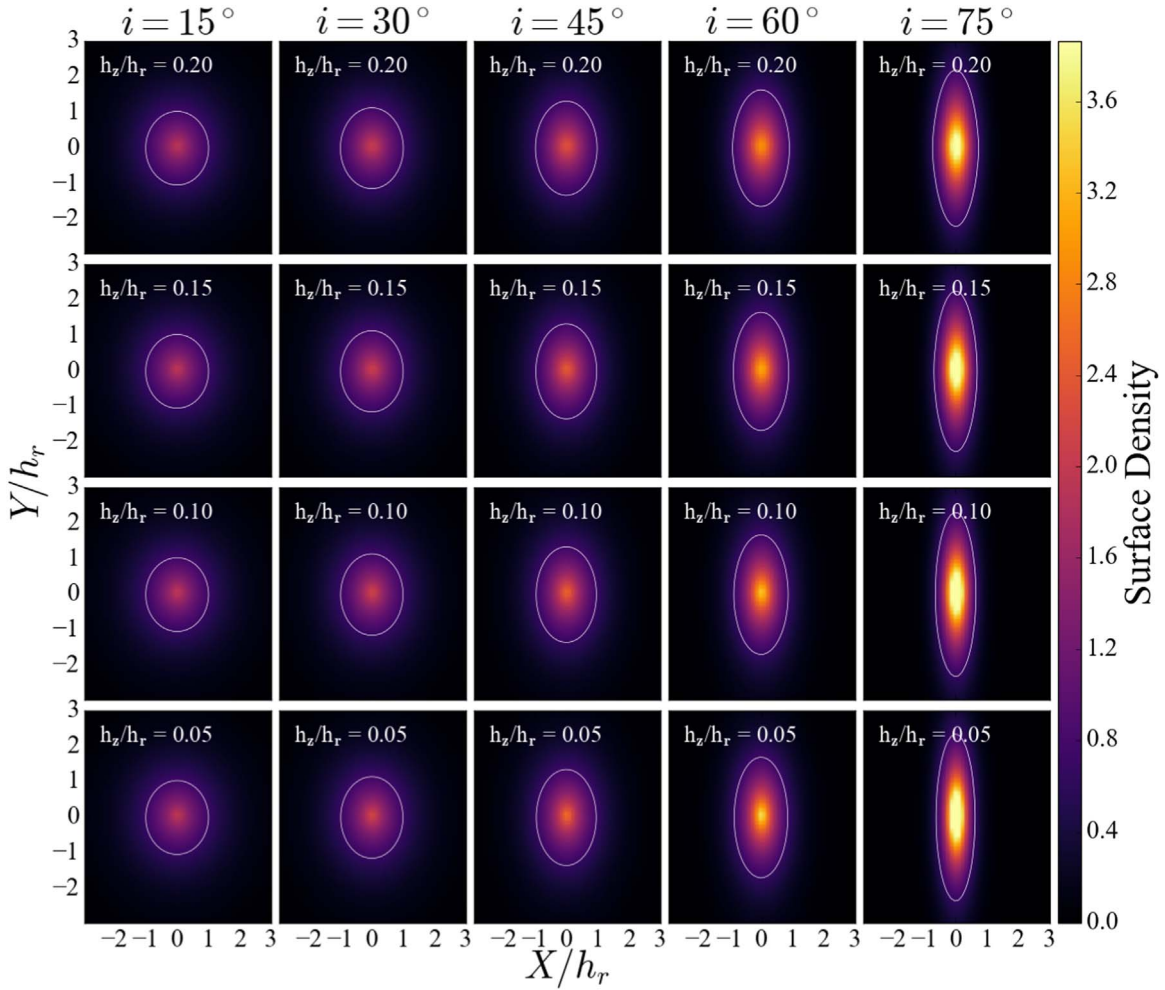


Figure 1. Maps of the apparent surface density for models of inclined, thickened disks, normalized to have a central surface density of unity when viewed face-on. The apparent inclinations of the model disks increase from left to right ($i = 15^\circ, 30^\circ, 45^\circ, 60^\circ,$ and 75°), and the disk thickness increases from bottom to top ($h_z/h_r = 0.05, 0.1, 0.15,$ and 0.2). The white ellipse is drawn at a constant apparent surface density, equal to that seen at $r = h_r$ for a face-on disk. At large inclination, this isodensity contour moves to larger effective radii, due to the increased path length through the disk.

$z = l \cos i$ and the radius is $r^2 = (x_0 + l \sin i)^2 + y_0^2$, where (x_0, y_0) is the Cartesian coordinates on the uninclined disk, assuming the major axis is oriented along the y -axis.

In Figure 1 we show maps of the projected stellar surface density, in a grid of inclination (varying along rows) and of disk thickness (i.e., h_z/h_r , varying along columns, with intrinsically thicker disks plotted toward the top). As expected, disks appear thinner when they are more highly inclined. This variation with inclination is less pronounced for intrinsically thicker disks, however, because such disks can never look truly thin, even at the highest inclinations. The impact of inclination and disk thickness on the apparent disk structure is summarized in Figure 2, where we plot the apparent axis ratio as a function of the inclination and h_z/h_r . The axis ratio is calculated for a fixed characteristic surface brightness level, chosen to be that observed for a face-on disk at a radius of $1.5h_r$, where the surface mass density of an exponential disk would have fallen by roughly a factor of five from the center but still be reliably measured in survey data. The typical radius where this is measured encompasses close to half of the mass of the disk, but is not so far out that warps and asymmetries are potentially significant. The loci in Figure 2 also assume that the disk is optically thin at the radius where b/a was measured, which is

not a bad assumption for long-wavelength observations at large radii.

Of greater interest is Figure 3, where we plot maps of the fraction of reddened stars ($f_{\text{red}} \equiv \Sigma_- / (\Sigma_+ + \Sigma_-)$), for model disks with the same inclinations and thicknesses as in Figure 1. At low inclinations, the fraction of stars behind the dust layer is essentially constant at $f_{\text{red}} = 0.5$. At high inclinations, however, the impact of the thickness of the disk can be seen. Off of the major axis, lines of sight pierce a range of radii, leading to significant differences in the fraction of reddened stars seen on either side of the major axis. In the half of the galaxy that is furthest from the observer, the stars in front of the dust layer come from the inner galaxy where the number density of stars is higher, leading to low reddening fractions. The variation in the reddening fraction across a disk is largest for high inclinations and for intrinsically thicker disks, both of which lead to longer path lengths and thus larger ranges of radii along a given line of sight.

We show the full variation of the reddening fraction in Figure 4, where we plot the approximate maximum value of f_{red} along the minor axis, calculated where the surface brightness falls to a value equal to that found at $3h_r$ for a face-on disk, which is far enough out that f_{red} can be assumed to be close to the maximum, while also expecting to be potentially measurable ($\sim 25 \text{ mag/arcsec}^2$ for an exponential Freeman disk). As

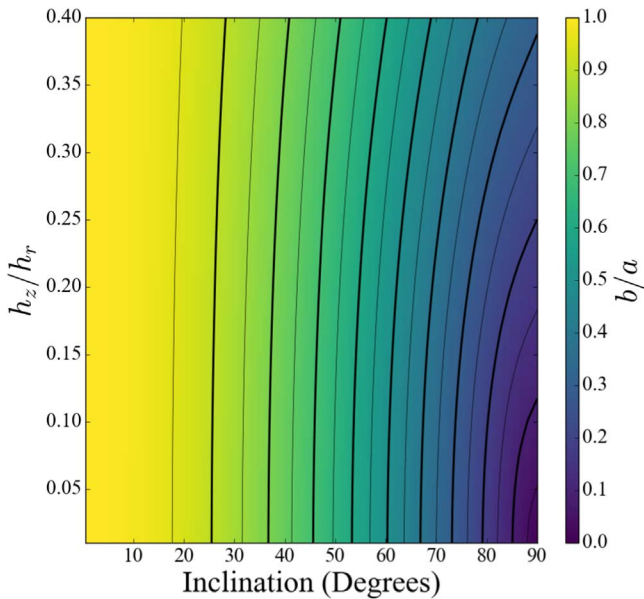


Figure 2. Axial ratio of model inclined, thickened disks, measured at the surface brightness corresponding to $r = 1.5h_r$ for a face-on disk. The heavy solid lines indicate the value of b/a in steps of 0.1 (i.e., $b/a = 0.1, 0.2$, etc.). The light lines indicate $b/a = 0.05, 0.15$, etc. For thicker disks and higher inclinations, the apparent axial ratio departs significantly from the naive expectation for an inclined, infinitely thin disk.

expected from Figure 3, the maximum observed value of f_{red} will be higher for more inclined and/or intrinsically thicker galaxies.

The above models point to ways in which the observed reddening fraction can be used to make new constraints on disk geometry. First, in any inclined galaxy, seeing obvious dust obscuration on only one side of the major axis trivially implies a thick stellar disk. Second, comparing Figures 2 and 4 suggests that the combination of measuring a disk’s apparent axial ratio and its maximum (or minimum) fraction of reddened stars will jointly constrain the disk’s thickness (through h_z/h_r) and inclination. We will take this approach below, after presenting measurements of f_{red} in M31.

3. Measuring the Fraction of Reddened Stars in M31

M31 is a massive, inclined, Sb galaxy, whose significant bulge and relatively low star formation rate places it in the “green valley” between active and quiescent galaxies (Mutch et al. 2011). Its star formation is driven by a significant, structured ISM that produces visible dust lanes, as shown in Figure 5. The left panel shows $100\ \mu\text{m}$ dust emission observed with Herschel (Fritz et al. 2012),¹¹ covering out to slightly beyond M31’s star-forming ring at a 10 kpc radius.¹² M31’s dust content is similar on either side of the major axis, although there are some modest differences between the northeastern (upper left) and southwestern (lower right) halves of the galaxy, largely due to the additional split in the ring in the southeast.

In contrast to the dust emission on the left, the blue optical image on the right shows a very different degree of asymmetry across the major axis. On the right (near) side of the galaxy, the dust lanes are very strong, even in regions where the absolute

amount of dust is comparatively low. The left (far) side of the galaxy, however, shows very little obvious dust extinction away from the major axis, in spite of there being ample dust. This morphology alone suggests that M31 has an internal geometry and viewing angle comparable to the models in the upper right quadrant of Figure 3.

We can quantify the position-dependent reddening in Figure 5 by measuring the fraction of reddened stars as a function of the position using the near-infrared (NIR) color–magnitude diagram (CMD) fitting technique described in Dalcanton et al. (2015). Briefly, we subdivide photometric data from the Panchromatic Hubble Andromeda Treasury (PHAT) survey¹³ (Dalcanton et al. 2012; Williams et al. 2014) into $\sim 6'' \times 6$ pixels (25 pc at the distance of M31). Within each pixel, we model the red giant branch (RGB) stars in the F110W–F160W CMD as a combination of an unreddened foreground and a reddened background population. We assume that the reddened stars have passed through a region with a log-normal distribution of dust columns, and then fit for the median extinction \tilde{A}_V , the width of the log-normal σ , and the fraction f_{red} of stars that are in the reddened component. Figure 6 shows an example comparing the measured stellar photometry to a model of the unreddened RGB (left) and to the best-fit model that contains both unreddened and reddened stars (right).

We characterize the posterior probability distribution function of each of these parameters using the Markov Chain Monte Carlo (MCMC) sampler `emcee` (Foreman-Mackey et al. 2013), assuming reasonable Bayesian prior probability distributions for f_{red} and σ . As is typical with Bayesian priors, the choice of the prior probability distribution only affects the fitted values of a parameter in regions where the constraints provided by the data are weak. Outside of these regions, the choice of prior has a negligible effect on the value of the fitted parameters.

The prior for f_{red} was assigned iteratively, as follows. We initially fit for f_{red} with a single prior to identify regions where the values of f_{red} were well constrained. We initially ran the fitting routine with a Gaussian prior centered at $f_{\text{red}} = 0.4$; we chose this peak to be less than 0.5 because the majority of the PHAT survey area was located on the side of M31 with less obvious dust reddening. This choice of a single, spatially-uniform prior is obviously inadequate (given the maps in Figure 3), but was sufficient to identify the regions where f_{red} was well measured, and then to use those regions to build a more appropriate spatially-variable prior for f_{red} . As discussed in Dalcanton et al. (2015), the uncertainties in f_{red} are the lowest where the median extinction \tilde{A}_V is the highest. In these regions, the reddened RGB is cleanly separated from the unreddened RGB on the CMD, making the value of f_{red} unambiguous. We therefore took all regions with $\tilde{A}_V > 1$ mag and then fit a tilted disk model to derive a positionally-dependent mean value of f_{red} . We then solved for the dust map parameters again using a prior that matched the expected value of f_{red} at each location. As expected, this change in prior had no noticeable effect on the values of f_{red} in high-extinction regions. In the analysis that follows, we include only high-extinction pixels ($A_V > 1.25$ mag), where the prior has minimal impact. Further details of these procedures and their associated uncertainties can be found in Dalcanton et al. (2015).

Throughout the fitting, we implicitly assume that stars are either in front of or behind the dusty gas. While this assumption

¹¹ Accessed from <https://irsa.ipac.caltech.edu/data/Herschel/HELGA/index.html>.

¹² Note that there is more dust at larger radii, but it is below the sky level of this image. Filtering in the reduction pipeline also misses some of the more extended emission, particularly at large radii (Clark et al. 2021).

¹³ All the Hubble Space Telescope (HST) data used in this paper can be found in MAST:10.17909/T91S30.

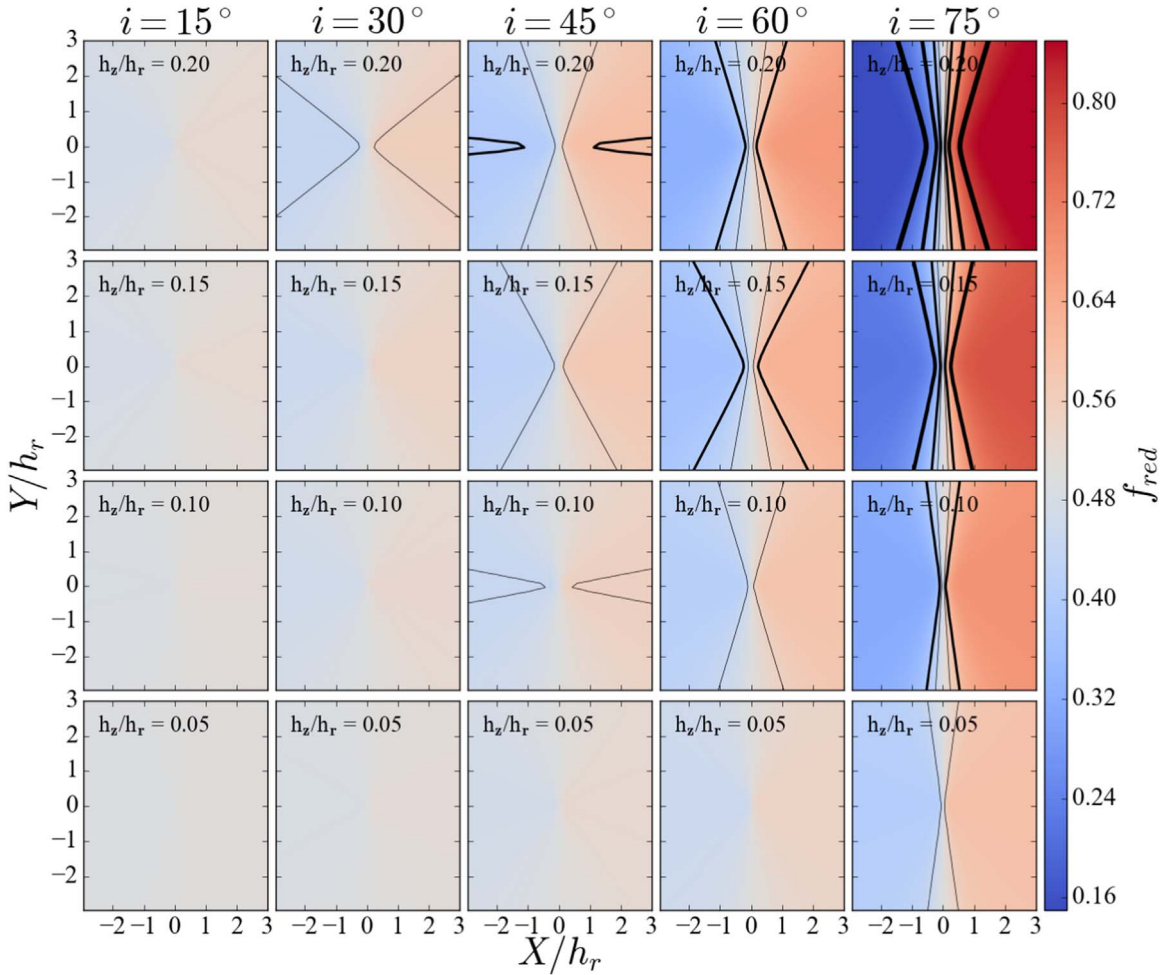


Figure 3. Maps of the apparent fraction of reddened stars for models of inclined, thickened disks where the dust is assumed to be confined to the midplane with negligible thickness compared to the stars (i.e., $h_z \gg h_{\text{dust}}$). The apparent inclinations of the model disks increase from left to right ($i = 15^\circ, 30^\circ, 45^\circ, 60^\circ,$ and 75°), and the disk thickness increases from bottom to top ($h_z/h_r = 0.05, 0.1, 0.15,$ and 0.2). As expected, the fraction of reddened stars is always 50% along the major axis, but deviates strongly perpendicularly, with the largest deviations seen for higher inclinations and intrinsically thicker disks. Contours indicate deviations of $\pm 5\%$, $\pm 10\%$, $\pm 20\%$, and $\pm 30\%$ relative to 50%, with thicker contours indicating larger deviations.

is unlikely to hold for young stars forming out of the gas, it is likely to be valid for the older stars that dominate the RGB. Empirically, we know that typical massive disk galaxies have clear dust lanes when viewed edge-on, strongly suggesting that the dusty, cold ISM is found in a layer that is much thinner than that of the stars. Quantitatively, in our own galaxy, the stellar disk has an exponential scale height $h_{z,\text{stars}}$ of 300 and 900 pc, for the thin and thick disks, respectively (Jurić et al. 2008). These heights can be compared to the scale height of the cold dust ISM, for which CO observations find a much smaller vertical half-width at half-maximum (HWHM) of $z_{\text{hwhm}} \sim 50$ pc (or $h_{z,\text{dust}} = 1.4 z_{\text{HWHM}} \approx 72$ pc) within the solar circle, with likely flaring by a factor of 2–4 in the outer disk (Heyer & Dame 2015; Marasco et al. 2017). Comparable ratios between the stellar and dust scale heights are seen in other massive disk galaxies (e.g., Xilouris et al. 1999).¹⁴ When viewed at high spatial resolution, the effective thickness of the cold dusty ISM may be even

smaller if the extinction along a line of sight is produced by individual molecular clouds (which have sizes of < 50 pc) within the thicker dust layer. As such, the treatment of the dust layer as being infinitely thin is unlikely to influence our results strongly.

3.1. Mapping the Fraction of Reddened Stars

Figure 7 plots the full map of the fraction of reddened stars f_{red} , restricted to points with well-measured values of f_{red} ($A_V > 1.25$ mag and $\Delta f_{\text{red}} < 0.06$, where Δf_{red} is half of the difference between the 16% and 84% percentile range for the MCMC-sampled posterior distribution of f_{red} , which would be equal to the standard deviation for a Gaussian distribution). In spite of the complexity of the extinction map presented in Dalcanton et al. (2015), and the independent analysis of each plotted pixel, the fraction of reddened stars varies smoothly and systematically across the disk. As expected, the fraction of reddened stars is 0.5 along the major axis, but diverges to much smaller and larger values with increasing distance from the major axis. There is a steady shift in the fraction of reddened stars from the near side of the disk (upper right) to the far side (lower left). On the near side, the fraction of reddened stars is very high, as would be expected from the optical morphology

¹⁴ Some high-latitude dusty clouds are seen in galaxies with high star formation rate intensities (e.g., Howk & Savage 1999; Rueff et al. 2013), and some diffuse dust may be associated with the thicker atomic gas layer (see their arguments in Wild et al. 2011), but the preponderance of clearly defined dust lanes (80% of edge-on Sloan Digital Sky Survey (SDSS) galaxies; Holwerda et al. 2012) suggests the majority of dust in massive galaxies is indeed associated with a thin layer confined to the midplane.

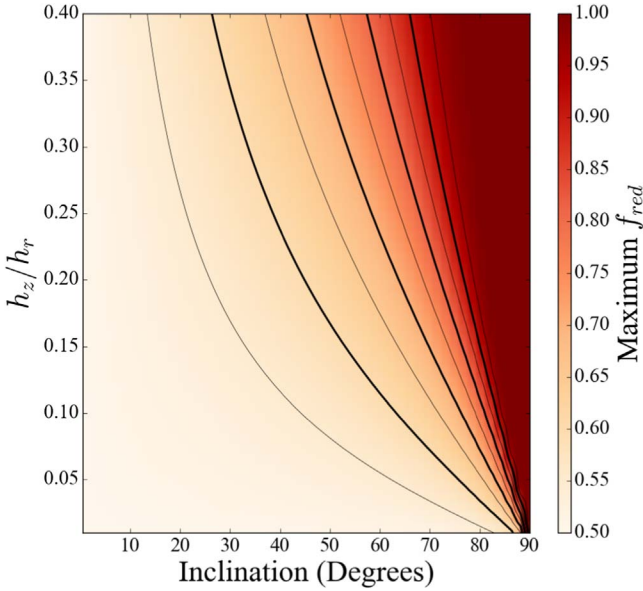


Figure 4. Maximum reddening fraction f_{red} for model inclined, thickened disks, measured along the minor axis at the surface brightness corresponding to $r = 3h_r$ for a face-on disk. The heavy solid lines indicate the value of f_{red} in steps of 0.1 (i.e., $f_{\text{red}} = 0.6, 0.7$, etc.). The light lines indicate $f_{\text{red}} = 0.55, 0.65$, etc. For thicker disks and higher inclinations, the maximum observed value of f_{red} deviates most strongly from the naive value of $f_{\text{red}} = 0.5$. The minimum value of f_{red} at each point is one minus the plotted value.

alone; this side of the disk shows clear dust lanes, which just graze the edge of the PHAT footprint. In contrast, on the far side of the disk (where there are no obvious strong dust lanes) the fraction of reddened stars is extremely low, with fewer than $\sim 20\%$ of the stars lying behind the dust layer.

We note that the result in Figure 7 is essentially by design, given that PHAT specifically targeted the quadrant of M31 that appeared the least affected by dust. That said, the low reddening fraction and the unobscured visual morphology does not actually suggest that there is no dust on the far side of the galaxy (e.g., Elmegreen & Block 1999), given that the extinction maps clearly show ample dust in this quadrant, as does the mid- and far-IR emission (e.g., Draine et al. 2014). Instead, the weakness of visible dust obscuration on the far side of the disk is the result of the geometrical effect we are exploiting in this paper.

The large observed range in f_{red} immediately suggests that the disk of RGB stars is not thin. If it were, then there would be only a modest radial range sampled along all lines of sight, and thus a comparable number of stars behind and in front of the thin dusty layer of the cold ISM. In such a case, f_{red} would not vary dramatically from 0.5, in sharp contrast to what we see here. In retrospect, the fact that even ground-based optical images of M31 show much stronger reddening on one-half of the galaxy is strong evidence for a thick disk as well, although not as quantitatively useful.

3.2. The 3D Structure of M31's Stellar Disk

To derive the disk thickness from the reddening map in Figure 7, we return to the distribution of maximum deviations from f_{red} , plotted in Figure 4 as a function of the inclination and h_z/h_r . The observed extremes of f_{red} identify a particular locus in the plot of the inclination and h_z/h_r . If we then constrain

M31's inclination from its observed axial ratio (Figure 2), we can derive the value of h_z/h_r for M31's stellar disk.

We identify the most extreme observed values of f_{red} by plotting histograms of f_{red} (blue) and $1 - f_{\text{red}}$ (red) from the far and near sides of the disk in Figure 8. For both quantities, we plot a subset of the points from Figure 7, after excluding regions at small deprojected radii ($r < 0.8$) and near the major axis, where we expect to find less extreme values of f_{red} based on the models shown in Figure 3. On the far side of the disk (low f_{red}), we selected points within $\pm 20^\circ$ of the minor axis ($160^\circ < \theta < 200^\circ$ where θ is the angular polar coordinate for the deprojected disk; see the transformations to polar coordinates described in the Appendix). The near side of the disk is not as well sampled, and we were forced to expand our selection to a wider range of angles ($\theta < 50^\circ$) to include the region of well-measured high values of f_{red} found in the 10 kpc star-forming ring. There are ~ 1400 points in the far side subsample and ~ 400 in the near side sample, and most are drawn from between 2 and $3.5h_r$, well into the regime where the value of f_{red} reaches its extremes (e.g., Figure 3).

The histograms in Figure 8 are clearly peaked at $f_{\text{red}} \approx 0.2$ on the far side and $f_{\text{red}} \approx 0.8$ on the near side, with very small tails toward $f_{\text{red}} = 0.5$, and a central width consistent with the uncertainties in f_{red} ($\langle \Delta f_{\text{red}} \rangle = 0.043$ and $\langle \Delta f_{\text{red}} \rangle = 0.044$ for the far and near sides, respectively). The tails are expected when admitting points away from the minor axis, and are more significant for the near-side data where we do not sample the large radius, minor axis behavior of f_{red} as well. We calculate robust means for each distribution and find $f_{\text{red}} = 0.214$ for the far side and $1 - f_{\text{red}} = 0.180$ for the near side. If we restrict the subset to even higher extinction regions ($A_V > 1.75$ mag), these values change to $f_{\text{red}} = 0.212$ and $1 - f_{\text{red}} = 0.186$. We have also experimented with different choices of signal-to-noise cuts and angular or radial extents, and find consistent answers with all plausible choices. The formal errors on the mean are quite small, but it is reasonable to assume that the true uncertainties are larger and potentially dominated by systematics, due to the small area sampled on the near side, and the possibility that fits are biased differently when f_{red} is high versus when it is low. As such, the difference between the two sides of the disk are likely to reflect the underlying uncertainty better, and we therefore adopt 0.303 ± 0.02 as the maximum observed deviation from $f_{\text{red}} = 0.5$, where the uncertainty reflects the likely amplitude of systematic effects, as indicated by the differences between the far and near sides.

We plot the locus corresponding to this deviation ($f_{\text{red,max}} = 0.803 \pm 0.02$) in Figure 9, as a function of the inclination and h_z/h_r . We now solve for h_z/h_r by constraining the inclination, using measurements of M31's disk ellipticity ($\epsilon = 1 - b/a$). A thorough analysis of 1D and 2D surface brightness fitting by Courteau et al. (2011) finds that $\epsilon = 0.73 \pm 0.01$ for M31's old stellar disk, which corresponds to $b/a = 0.27 \pm 0.01$. Joint kinematic plus photometric decomposition in the I band by Dorman et al. (2013) find $\epsilon = 0.725 \pm 0.005$, in excellent agreement with Courteau et al. (2011). We adopt the more generous $\Delta\epsilon = \pm 0.01$ range from Courteau et al. (2011) to be conservative in our final estimate of the uncertainty on h_z/h_r . In Figure 9 we reproduce the loci that trace how this range of b/a depends on inclination and h_z/h_r , based on the earlier results in Figure 2.

The intersection of the loci for the observed maximum f_{red} and the disk axial ratio places a tight joint constraint on the

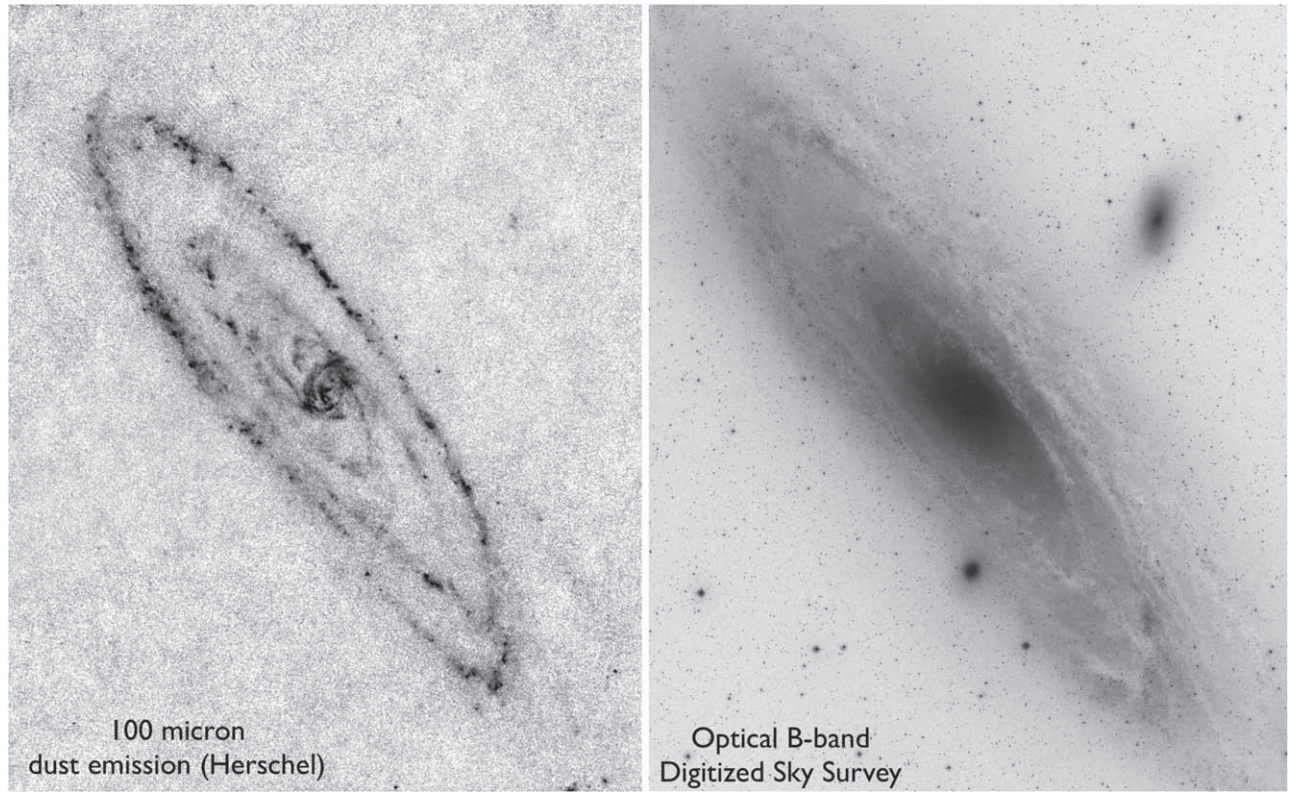


Figure 5. Comparison between a Herschel Photodetector Array Camera and Spectrometer $100\ \mu\text{m}$ image of emission from M31’s dust (left; from Fritz et al. 2012), and an optical B -band image from the Digitized Sky Survey (right). The Herschel image shows that M31’s dust content is similar on either side of the major axis. However, the stellar extinction from the dust is far more apparent on the northern (upper) half of the galaxy, leading to prominent dust lanes in the optical image. The PHAT survey footprint roughly covers the upper left quadrant of the image, extending further out in radius beyond the prominent 10 kpc ring seen in the Herschel image.

inclination and thickness of M31’s disk. The inclination is $77^\circ \pm 0.5$, which is excellent agreement with the values derived from the tilted-ring fitting of M31’s HI velocity field over the radii where we have measured f_{red} (Chemin et al. 2009; Corbelli et al. 2010).

Figure 9 also places good constraints on the vertical scale height h_z relative to the radial scale length h_r . We find $h_z/h_r = 0.14 \pm 0.015$, indicating the scale length of the disk is between 6.5 and 8 times larger than the scale height. This ratio applies only to the older stellar disk, as f_{red} was measured from NIR-bright RGB stars. It also does not differentiate between any possible kinematic and/or metallicity subcomponents among the RGB stars themselves (such as the thin and thick components identified by Collins et al. 2011 or the “kicked up” disk stars identified by Dorman et al. 2013), and instead reflects the properties of whichever subpopulation dominates the RGB stars.

We can convert the measured value of h_z/h_r into the actual scale height h_z by using measurements of h_r . We summarize some of the most relevant existing measurements of h_r in Table 1, focusing on analyses at longer wavelengths where the light is more likely to be dominated by the RGB stars used in the measurement of f_{red} . We also include measurements of h_r that directly analyze the density of RGB stars (e.g., Choi 2016). Although some individual papers quote high-precision measurements for h_r , the true accuracy is much poorer, largely because of the complexity of M31’s true structure, which features multiple central spheroids (e.g., Beaton et al. 2007), bars (e.g., Athanassoula & Beaton 2006; Choi 2016; Blańa Díaz et al. 2017; Opitsch et al. 2018), and an overdensity of

light and stars at the 10 kpc ring (e.g., Courteau et al. 2011; Dalcanton et al. 2012). We adopt $h_r = 5.5 \pm 0.5$ kpc as a realistic estimate of the appropriate scale length and its uncertainty. With this, we find

$$h_z = 0.77 \pm 0.08 \text{ kpc} \left(\frac{h_r}{5.5 \text{ kpc}} \right). \quad (2)$$

If we consider the uncertainties on h_z/h_r and h_r as ranges allowed by systematic errors, then we expect h_z to fall in the range 625–930 pc. We note that this is substantially larger than the likely scale height of the cold dusty gas, supporting the validity of treating the dust as a thin screen within the stellar disk.

4. The Thickness of M31’s Stellar Disk in Context

The measurements presented in Section 3.2 indicate that M31’s stellar disk is moderately puffy ($h_r/h_z \approx 7.1$) and thick, with half of the stellar disk mass lying more than $\pm 0.53 \pm 0.05$ kpc above or below of the midplane (assuming the half-height $z_{1/2} = 0.693h_z$ for an exponential disk, with $h_z = 0.77$ kpc). We now place these measurements in the larger context of what is known about the structure of disk populations in the Milky Way, and in larger samples of edge-on galaxies.

4.1. Comparison to the Milky Way

Although the exact scale height of the Milky Way’s disk remains somewhat uncertain, scale heights as large as we

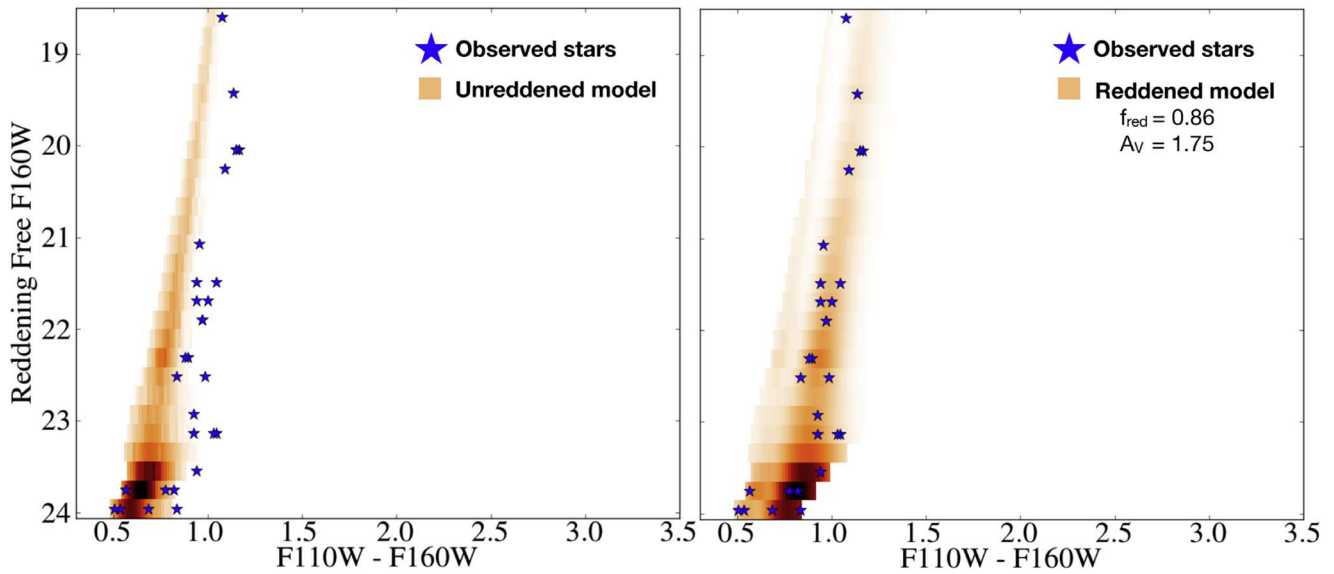


Figure 6. Representative comparison between the observed NIR stellar photometry of the RGB in a single analysis pixel (blue stars), to the expected model of the unreddened RGB (left) and to the best-fit model where a fraction f_{red} of the RGB stars are allowed to be behind a layer of dust with a log-normal distribution of extinction characterized by a median A_V (right). This region, drawn from the northern half of the major axis, requires a large fraction of the stars to be reddened, consistent with the visual presence of dust lanes in Figure 5. The F160W magnitude has been transformed to a reddening-free quantity, such that dust extinction and reddening move stars only to the right (Dalcanton et al. 2015).

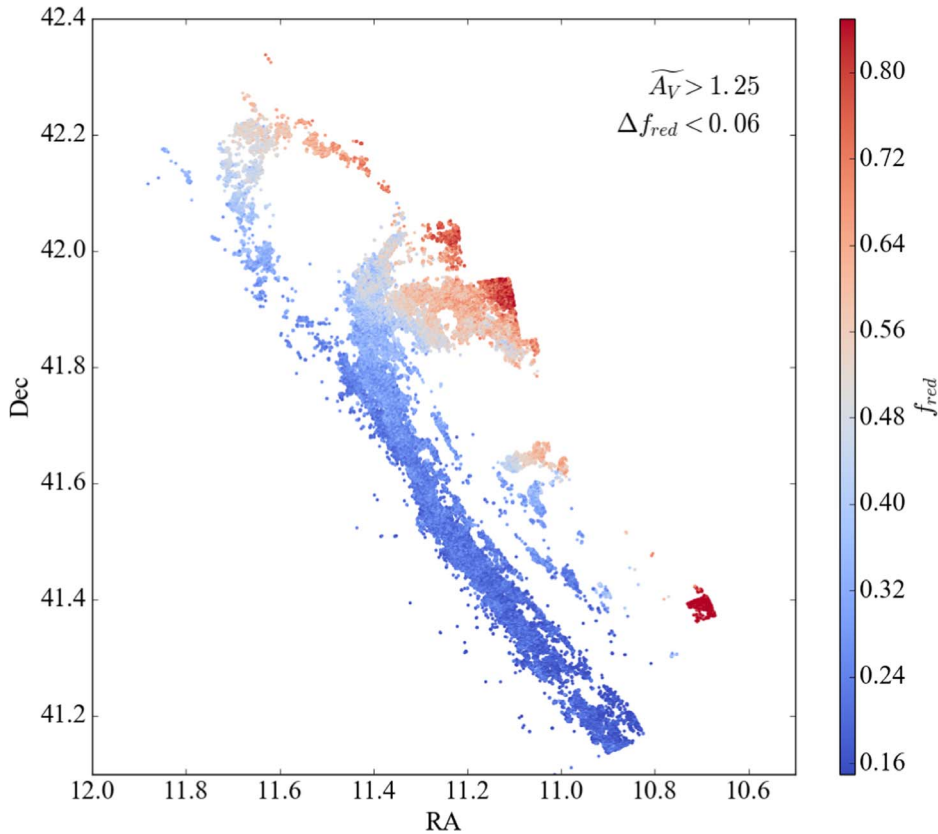


Figure 7. Map of the fraction of reddened stars f_{red} , restricted to high-extinction ($A_V > 1.25$ mag) regions with well-measured values of f_{red} ($\Delta f_{\text{red}} < 0.06$). There is a clear gradient in the fraction of reddened stars from the far side to the near side of the disk (i.e., left to right). The majority of the PHAT survey area, which was initially targeted to avoid M31’s dust lanes, has fewer than $\sim 25\%$ of its old stellar population behind the dusty ISM. The center of M31 is in the lower right, at R.A. ≈ 10.68 and decl. ≈ 41.27 .

measured for M31 have never been reported for the Milky Way’s thin disk. The synthesis of Milky Way structural measurements by Bland-Hawthorn & Gerhard (2016) argues

for a metal-rich “thin” disk component that is more than a factor of two smaller than what we find in M31 ($h_{z,\text{thin}} \approx 300\text{--}350$ pc from photometric studies, or smaller

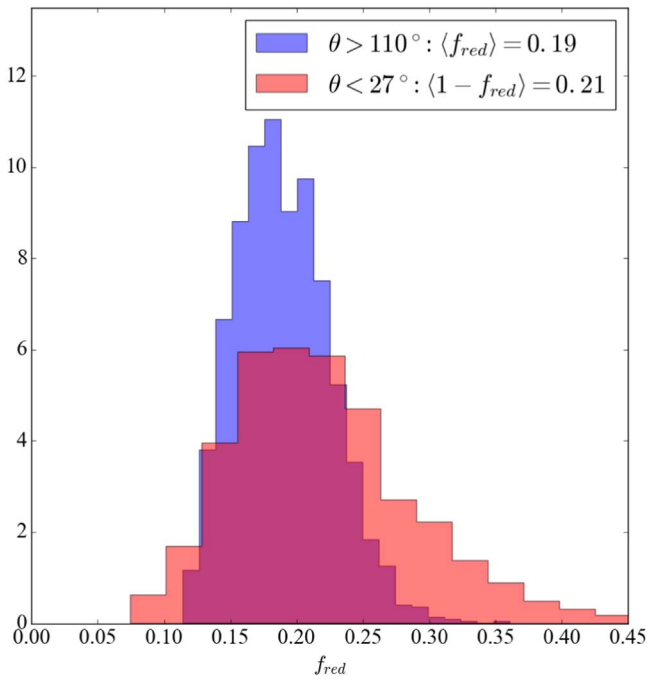


Figure 8. Extremes of the fraction of reddened stars f_{red} , using the same high-quality measurements plotted in Figure 7. The minimum values of f_{red} (blue histogram) are calculated in regions roughly along the minor axis ($\theta > 110^\circ$), and the maximum values (plotted as $1 - f_{\text{red}}$; red histogram) are calculated at $\theta < 27^\circ$, due to lack of data along the minor axis for the highly reddened side of the disk. These maximum values are taken from much closer to the major axis, and so are not expected to have reached their asymptotic values, unlike for the minimum values of f_{red} ; this limitation is manifested as the tail to larger values of $1 - f_{\text{red}}$ in the red histogram. In spite of the poorer sampling of regions with high f_{red} , the values of f_{red} on the obscured, near side of the disk are in good agreement with expectations from the well-sampled far side, given that the mean $f_{\text{red}}(\theta > 110^\circ) \approx 1 - f_{\text{red}}(\theta < 27^\circ)$, after culling the obvious tails at $f_{\text{red}} > 0.27$ and $1 - f_{\text{red}} > 0.32$.

values of $h_{z,[\text{Fe}/\text{H}] > -0.3} \approx 240\text{--}270$ pc when subdividing populations on metal abundance (e.g., Bovy et al. 2012b)).

In contrast, measurements of the scale height of the Milky Way’s thick and/or metal-poor disk are comparable to that seen for M31’s RGB stars ($h_{z,\text{thick}} \approx 700\text{--}1200$ pc or $h_{z,[\text{Fe}/\text{H}] < -0.25} \approx 690\text{--}770$ pc; Bovy et al. 2012b; Bland-Hawthorn & Gerhard 2016). We demonstrate this correspondence in Figure 10, where we plot the vertical scale heights of the monoabundance populations from Bovy et al. (2012b) and outline the metallicity subpopulations that have thicknesses consistent with that seen in M31. Only by looking at metal-poor subpopulations with $[\text{Fe}/\text{H}] \lesssim -0.6$ and α -enhancements of $[\alpha/\text{Fe}] \gtrsim 0.2$ do we find Milky Way subpopulations with comparably thick disks. The larger thickness of M31’s stellar disk persists even if we consider the possibility that we have overestimated h_z by multiplying the measured value of h_z/h_r by too large a value of h_r . Among modern measurements, there are no disk scale lengths smaller than $h_r \approx 5$ kpc (see Table 1). If we adopt this extreme value of the scale length, it would only drop our estimate of h_z to 700 pc, which is still more comparable to the Milky Way’s modest thick disk than its dominant thin disk.

For an alternative comparison, we can avoid the complication of scaling by an uncertain value of h_r by instead directly comparing our measured value of h_z/h_r to the same ratio in the Milky Way (although the latter is affected by significant

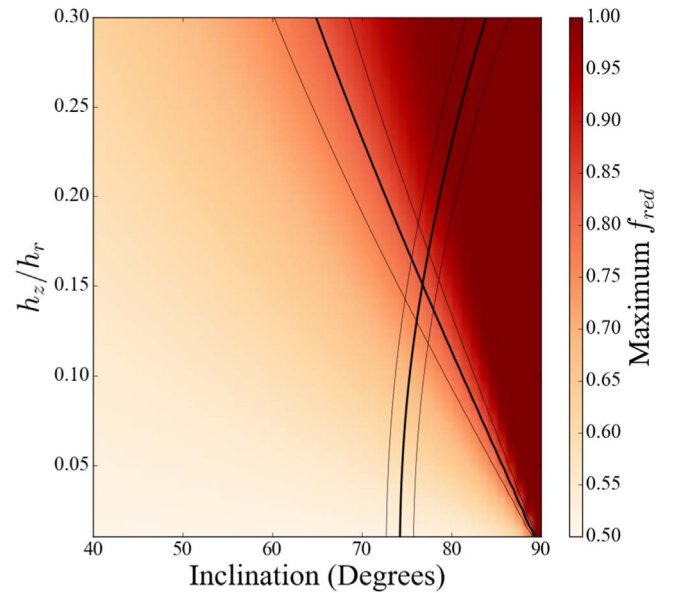


Figure 9. Observational constraints on the maximum reddening fraction f_{red} and the observed axial ratio for model inclined, thickened disks. The background color indicates the maximum reddening fraction as shown in Figure 4 (i.e., measured along the minor axis at the surface brightness corresponding to $r = 3h_r$ for a face-on disk). One set of contours indicates the typical maximum value of $f_{\text{red}} = 0.803 \pm 0.02$ observed in M31 (equivalent to the minimum values of $f_{\text{red}} = 0.197 \pm 0.02$; see Figure 8). The other set of contours indicates the range of measured axial ratios from Courteau et al. (2011; $b/a = 0.27 \pm 0.01$), derived from their reported ellipticities ($\epsilon = 0.73 \pm 0.01$), corresponding to an inclination of $i = 74^\circ$ for an infinitely thin disk. The intersection of these two independent measurements favors a typical disk thickness in the range of $h_z/h_r \approx 0.15$ and a larger true inclination of $i \approx 77^\circ$, which is in better agreement with the somewhat larger estimates of the inclination from the tilted-ring fitting of M31’s HI velocity field (Chemin et al. 2009; Corbelli et al. 2010).

uncertainties in the Milky Way’s h_r). The current best estimates of $h_z = 300 \pm 50$ pc and $h_r = 2.6 \pm 0.5$ kpc from Bland-Hawthorn & Gerhard (2016)’s review give $h_z/h_r = 0.11^{+0.05}_{-0.03}$ for the Milky Way’s dominant thin disk, which is more than 30% smaller than the dominant population in M31. We can also compare to the axial ratios of the monoabundance populations in Bovy et al. (2012a), as shown in Figure 10. Their thin disk analog subpopulation (high-metallicity, solar α -enhancement, which dominates the Milky Way stellar disk) has typical thicknesses of $h_z/h_r = 0.064\text{--}0.071$, which is twice as flattened as we have measured in M31. At the other extreme, their thick disk analog (low-metallicity, α -enhanced) subpopulation has intrinsic thicknesses of $h_z/h_r = 0.31\text{--}0.43$, which is consistent with measurements from RR Lyrae stars (Mateu & Vivas 2018) in the Milky Way, but is more than twice as puffy as M31’s dominant stellar disk. Thus, while M31’s disk has a comparable absolute scale height to the Milky Way’s metal-poor thick disk subpopulation, its proportions are somewhat more disk, although not nearly as flattened as the Milky Way’s dominant metal-rich stellar disk.

We note that unlike in M31, the Milky Way’s thicker components only make up a small fraction of its surface density at the Solar circle. Bland-Hawthorn & Gerhard (2016) argue for $f_{\text{thick,MW}} \approx 12\% \pm 4\%$, based on the available literature considered in their review. A slightly higher fraction of thick disks stars is suggested by the monoabundance populations from Bovy et al. (2012b, $\lesssim 30\%$ of the stellar mass; see Figure 10),

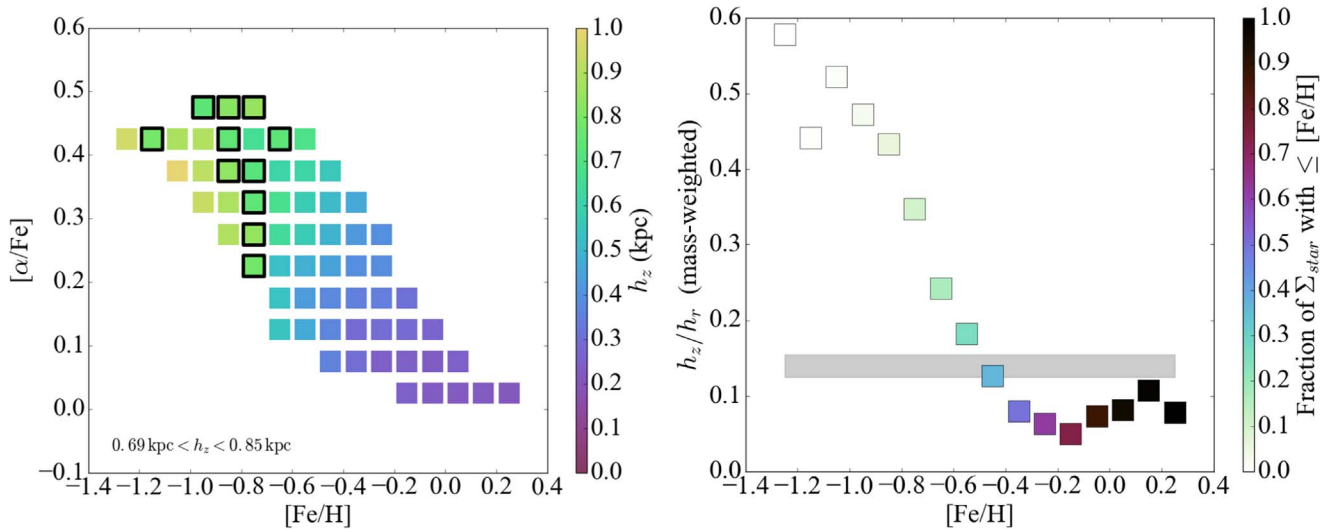


Figure 10. Comparison between the structure of M31’s RGB disk and the structure of the Milky Way’s monoabundance populations from Bovy et al. (2012a). (Left) Monoabundance populations in $[\text{Fe}/\text{H}]$ vs. $[\alpha/\text{Fe}]$, color coded by their vertical scale height at the solar circle. Populations whose scale height falls in the range allowed by the data in M31 are outlined in black. Only low-metallicity, α -enhanced Milky Way populations have scale heights comparable to those we see in M31. (Right) The axial ratio of the monoabundance subpopulations as a function of $[\text{Fe}/\text{H}]$ calculated as a mass-weighted average of h_z/h_r over $[\alpha/\text{Fe}]$ at fixed $[\text{Fe}/\text{H}]$. Points are color coded by the fraction of the integrated local stellar density found in populations with metallicities equal to or lower than $[\text{Fe}/\text{H}]$. The horizontal bar show the likely range of h_z/h_r for M31’s stellar disk. Only low-metallicity populations ($[\text{Fe}/\text{H}] \lesssim -0.5$) that make up $\sim 30\%$ of the Milky Way disk are as puffy as the M31 disk.

Table 1
M31 Disk Exponential Scale Length Measurements at Long Wavelengths

h_r (kpc)	Bandpass ^a	Reference	Notes
5.3 ± 0.5	$3.6 \mu\text{m}$	Courteau et al. (2011)	Variety of methods including 2D bulge+disk fitting and 1D fits to major and minor axis wedges at a fixed position angle
5.91 ± 0.27	$3.6 \mu\text{m}$	Seigar et al. (2008)	Fitting 1D profile from ellipse-fitting surface brightness profile
5.09–5.91	$3.6 \mu\text{m}$	Seigar et al. (2008)	Rotation curve fitting with different models
5.76 ± 0.1	<i>I</i>	Dorman et al. (2013)	Joint kinematic+photometric modeling of velocities+image
5.26 ± 0.01	W1	Choi (2016)	2D bulge+disk fitting of Wide-field Infrared Survey Explorer mosaic
5.56 ± 0.45	...	Choi (2016)	2D bulge+bar+disk fitting of RGB star counts from PHAT data
5.0–5.5	...	Williams et al. (2017)	Stellar mass profiles derived from HST optical+NIR CMDs
5.1 ± 0.1	...	Ibata et al. (2005)	RGB star counts in the outer disk (20–40 kpc)

Note. All scale lengths calculated at a distance of 785 kpc.

^a $3.6 \mu\text{m}$ images taken from Spitzer Infrared Array Camera images by Barmby et al. (2006) and *I*-band images taken from Choi et al. (2002) unless otherwise noted.

but the thick disk fraction is always well below 50% of the disk mass. In contrast, our measurement of the structure of M31’s disk must reflect the stellar populations that dominate the RGB, and would therefore be insensitive to a trace population that only made up a small fraction of the RGB stars. The most direct comparison can be made by ignoring any subdivision of the Milky Way into different disk components; when doing so, Bovy & Rix (2013) find that the integrated stellar disk has an exponential scale height of $h_{z,\text{MW}} \approx 400$ pc (based on the total stellar mass distribution calculated in Bovy et al. 2012a), which again is close to a factor of two smaller than what we find in M31.

In summary, by multiple measures, M31’s older stellar disk is substantially thicker than the disk of the Milky Way, in spite of the fact that it has an age and metallicity comparable to the Milky Way’s thin disk (mean age of ~ 4 Gyr and metallicities in the range of $[\text{Fe}/\text{H}] \approx 0$ in the inner disk and $[\text{Fe}/\text{H}] \approx -0.3$ in the outer disk based on work by Dorman et al. 2015 and Gregersen et al. 2015).

4.2. Comparison to other Galaxies

In addition to comparing to the Milky Way, we can compare our measurement of h_z/h_r for M31’s RGB stars to structural measurements of edge-on disks. These measurements are necessarily more uncertain than measurements in the Milky Way, due to the strong effect of dust opacity. Dust in the midplane of edge-on galaxies will typically be optically thick, such that the measured surface brightness profiles do not reflect the true stellar density. Even ignoring the effects of dust, typical extragalactic observations frequently lack the spatial resolution to accurately fit the shape of the vertical surface brightness distribution near the midplane, unless the galaxies are very close. Finally, there is also evidence that the widely-used practice of fitting the observed 2D profiles yields systematically different results than fitting true 3D models (e.g., Bizyaev et al. 2014). We attempt to minimize these issues by focusing on the subset of studies that use NIR observations of very nearby galaxies, but recognize that we are unlikely to have eliminated the significant uncertainties, making the

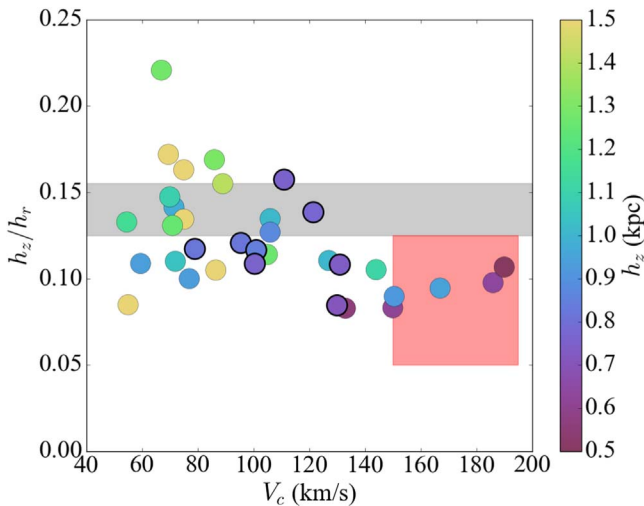


Figure 11. Comparison between the structure of M31’s RGB disk and the structure of edge-on disks from observations in the NIR. Circular points are disk axial ratios (h_z/h_r) as a function of the galaxy circular velocity, color coded by scale height for the single-disk fits from Yoachim & Dalcanton (2006), based on fitting 2D models to K_s imaging data for bulgeless galaxies selected from Karachentsev et al. (1993)’s Flat Galaxy Catalog; points with heavy black outlines have values of h_z within range of the values compatible with our results for M31. The red rectangular region indicates the range of h_z/h_r found for 2D fits of either 2MASS or Spitzer imaging of edge-on galaxies with bulge-to-total ratios greater than zero by Mosenkov et al. (2015). The vertical extent of this red region is also indicative of typical values for the Milky Way (e.g., Figure 10). The shaded gray region indicates the range compatible with observations in M31. The massive ($V_c > 120 \text{ km s}^{-1}$) bulgeless galaxies from Yoachim & Dalcanton (2006) have structural parameters consistent with the Milky Way’s dominant metal-rich disk (Figure 10) but are systematically flatter than what we observe in M31. The disks of galaxies with bulges from Mosenkov et al. (2015) are likewise better analogs of the Milky Way than M31.

comparison with the Milky Way probably the most direct analog of the measurements made in M31.

We first compare our results to structural parameter fits of K_s -band images of edge-on bulgeless galaxies in Yoachim & Dalcanton (2006). Although Yoachim & Dalcanton (2006) eventually decompose galaxies into thick and thin components, we focus on the fits to models of a single edge-on double exponential disk, which offer the best analog of the measurement we have made in M31, as both measurements are dominated by structure of stars on the RGB.

In Figure 11 we plot the ratio of scale height to scale length (h_z/h_r), as a function of the galaxy circular velocity, color coded by the vertical scale height in kiloparsecs. The range of h_z/h_r consistent with the observations in M31 (gray bar in Figure 11) is noticeably larger than the Yoachim & Dalcanton (2006) measurements for massive disks ($V_c > 120 \text{ km s}^{-1}$), suggesting that M31’s stellar disk is puffier than typical massive disks in very late-type galaxies. Although these galaxies may not be ideal analogs for an Sb galaxy like Andromeda, they are consistent with the properties of the Milky Way’s dominant metal-rich disk (Figure 10).

We may find better analogs of M31 among the more diverse sample analyzed by Mosenkov et al. (2015), also using 2D fitting comparable to that in Yoachim & Dalcanton (2006), but for Two Micron All Sky Survey (2MASS) K_s -band and Spitzer 3.6μ imaging from the S⁴G survey. The red rectangular region in Figure 11 indicates the range of h_z/h_r found for galaxies with bulge-to-total luminosity ratios greater than zero. As with

the bulgeless galaxies, M31 is again an outlier in terms of its intrinsic axial ratio.

In total, the comparison of M31 to the measurements in Figure 11 suggest that M31’s thickness is unusual in the context of disk galaxies in general, not just compared to the Milky Way.

4.3. Other Indicators of M31’s Thickened Disk

Our measurement of M31’s disk is fully consistent with its other observed features. First, M31’s stellar disk has a high velocity dispersion, as would be needed to support a vertically extended disk. In a series of papers Dorman et al. (2012, 2013, 2015) used Keck spectroscopy of stars selected in the PHAT footprint to measure a high velocity dispersion for M31 RGB stars. They found a line-of-sight velocity dispersion of $\sim 90 \text{ km s}^{-1}$ over much of the disk beyond 10 kpc, rising to 120 km s^{-1} in the inner disk at 5 kpc. High velocity dispersions were further confirmed when using more detailed chemodynamic selection of the disk population (Escala et al 2023). Large velocity dispersions are also seen in the population of disk planetary nebulae, both directly (e.g., Bhattacharya et al. 2019), and as indicated by their significant rotational lag due to asymmetric drift (Merrett et al. 2006).

Unfortunately, the line-of-sight velocity dispersion is not a direct measure of the vertical velocity dispersion, which is the component that is most relevant to disk thickness. However, although the full 3D velocity ellipsoid is unknown in M31, we can use the Milky Way as a model to show that the vertical component is likely to also be high. In the Milky Way, the radial velocity dispersion is typically a factor of $1.4\text{--}2.1\times$ larger than the vertical velocity dispersion (e.g., Büdenbender et al. 2015; Sharma et al. 2021), which would make the vertical velocity dispersion $\sim 43\text{--}57 \text{ km s}^{-1}$ if M31’s velocity ellipsoid were similar the Milky Way’s, assuming the Dorman et al. (2015) line-of-sight measurement is dominated by the radial component. For comparison, the only component of the Milky Way with such a high vertical velocity dispersion is the most metal-poor, α -rich subpopulation ($\sigma_z \approx 47 \text{ km s}^{-1}$, versus $\sigma_z \approx 19 \text{ km s}^{-1}$ for the metal-rich, α -poor disk; Büdenbender et al. 2015).

We note that an earlier paper by Collins et al. (2011) also argued for a thick disk in M31 on the basis of stellar kinematics, largely measured in the outer disk ($\gtrsim 15 \text{ kpc}$, with the exception of one field at $\sim 10 \text{ kpc}$). They decomposed their measured velocity distributions into a low velocity dispersion thin and a high velocity dispersion halo component, and then found evidence for an intermediate dispersion rotating component that lagged the rotation of the thin disk by $\sim 50 \text{ km s}^{-1}$, which they then identified as a thick disk. However, despite the similarity in nomenclature, it is unlikely that the thick disk in Collins et al. (2011) is strictly analogous to the overall thickened disk we measure here. The Collins et al. (2011) thick disk is a single subcomponent added to a dominant thin disk with a $\sim 36 \text{ km s}^{-1}$ line-of-sight velocity dispersion, whereas both we and Dorman et al. (2015) find that the majority of the old RGB stellar population is suggestive of a hot, thickened component.

We suspect that a substantial part of the difference in interpretation might be traced to the larger mean radius of Collins et al. (2011), and to a lesser degree to the nonoverlapping analysis regions (where PHAT covers the northeast and Collins et al. (2011) the southwest). While the

majority of the Collins et al. (2011) fields have 22–35 km s⁻¹ velocity dispersions for their thin disk component, their two innermost fields have thin disk dispersions of 55–69 km s⁻¹, which is much closer to the values in Dorman et al. (2015) and consistent with the earlier ~50 km s⁻¹ velocity dispersions for the extended disk reported by Ibata et al. (2005). Collins et al. (2011) also report that they had difficulty isolating a clean thick disk component in the inner regions, which would be consistent with Dorman et al. (2015) and our conclusion that the RGB stars in the inner disk are primarily in a thick component.

Alternatively, some of the differences in the characteristic velocity dispersion could be due to differences in methodology. Collins et al. (2011)’s velocity dispersions are based on decompositions of the velocity histogram into multiple components using a Gaussian mixture model and/or identifying the thick disk as those stars that are not well fit by a disk or halo component. In contrast, Dorman et al. (2015) reports the weighted second moment of the entire line-of-sight velocity distribution. The former method (which was needed to deal with the larger importance of the halo at large radii) will always produce smaller velocity dispersions than treating the entire distribution with a single component (which is well-justified in the inner disk covered by Dorman et al. 2015, as commented on in Dorman et al. 2012).

We also considered whether the different conclusions about velocity dispersions could be traced to differences in stars used in the analyses. While Dorman et al. (2015) analyze RGB and AGB stars separately, Collins et al. (2011) analyzes all the red stars within a magnitude range that likely contains some degree of contamination from younger AGB stars (compare Figure 7 of Collins et al. 2011 to Figure 5 of Dorman et al. 2015). Although the strong age-dependent velocity dispersion seen in Dorman et al. (2015) could lead to some degree of bias, we suspect this contamination is modest and unlikely to produce the difference in the velocity dispersion.

In addition to M31’s thickened disk being compatible with the large velocity dispersion measured in the PHAT footprint, it is also nicely consistent with the merger history models recently proposed by D’Souza & Bell (2018b) and Hammer et al. (2018). In these models, M31 experienced a major <4:1 gas rich merger ~2 Gyr ago, producing a high velocity dispersion stellar disk in the simulations of Hammer et al. (2018). Because the Hammer et al. (2018) model was tuned to in part reproduce the high disk velocity dispersion measured by Dorman et al. (2015), its agreement with the data is not surprising. However, their simulations do show a strong gradient in disk velocity dispersion, such that the outer disk sampled in Collins et al. (2011) would be lower velocity dispersion than the inner regions sampled by Dorman et al. (2015). This difference may well arise from the differing contributions of the two progenitors to the two survey areas. In the Hammer et al. (2018) models, the outer disk is dominated by stars pulled from the primary progenitor, whereas the PHAT survey region contains a strong mixture of both the primary and secondary progenitors.

Finally, there are tentative hints of a thickened disk in the 3D chemical structure of M31, as inferred from “made-to-measure” chemo-dynamical modeling of integral field spectroscopy of M31 (Gajda et al. 2021). The authors find flaring in the overall metallicity, and a tendency toward larger α -enhancement at larger scale heights, which they argue is consistent with thickening due to a major merger as advocated for by Hammer

et al. (2018), D’Souza & Bell (2018b), and Bhattacharya et al. (2019).

5. Implications

The geometric confirmation that the majority of M31’s stellar disk is thick is perhaps not terribly surprising, given the violent merger history visible in M31’s extended halo, the high disk velocity dispersion measured for its intermediate and old stellar populations, and the strong evidence for a recent, global elevation of the star formation rate 2–3 Gyr ago (Bernard et al. 2015; Williams et al. 2015). That said, there are a number of interesting implications of having a thickened stellar disk for M31, and for potentially identifying thickened disks in other systems.

5.1. Identifying Candidate Thickened Disks

The basic technique employed in this paper points toward an efficient mechanism for finding equivalently thickened systems. Inspection of the models in Figure 3 show that at fixed inclination, the difference in apparent reddening on either side of the major axis is an indicator of disk thickening. Identifying moderately inclined galaxies that show a dust lane on only one side would therefore be a straightforward way to identify candidates for similarly thickened disks.

Inferring the exact value of disk thickening would require subsequent modeling to calculate the actual reddening of dust lanes in the imaging data, along with an estimate of the total dust column from its emission at mid- and far-infrared wavelengths. This approach was used in a prescient paper¹⁵ by Elmegreen & Block (1999) to explain the highly asymmetric $V-K$ profile of the galaxy NGC 2841, and other similar galaxies like M64 (the “evil eye” galaxy NGC 4826) and NGC 3521. For some applications, it may be sufficient to only characterize one’s lower limits for h_z/h_r , without the need for any additional modeling beyond setting selection criteria.

5.2. Metallicity Gradients

M31’s thickened stellar disk can potentially wash out radial gradients in the disk. In a thickened disk, lines of sight away from the major axis probe a large range of radii, and as such, any intrinsic gradients in the disk will tend to be averaged out. We show the amplitude of this effect in Figure 12, which shows the mass-weighted dispersion in radii probed at each position in an inclined, thick double exponential disk. For galaxies with parameters like M31’s (second panel from the top on the far right), a single line of sight can sample stars from roughly $\pm 1.5h_r$ in disk radius.

The effect shown in Figure 12 may partially explain the lack of any strong radial gradient seen in the planetary nebula (PNe) metallicity distribution (e.g., Jacoby & Ciardullo 1999; Sanders et al. 2012; Bhattacharya et al. 2019; Kwitter et al. 2012; Balick et al. 2013, 2017) as well as its large scatter. These intermediate age ($\gtrsim 5$ Gyr; see Balick et al. 2017) stars are likely to be distributed similarly to the RGB stars used in this paper, and the long path length through the stellar disk will tend to blend PNe from multiple radii into a single sightline, erasing whatever intrinsic metallicity gradient survived M31’s likely major merger. This merger-driven mixing and the projection

¹⁵ We gleefully note that this is also the first astronomical paper to use “bogus” in the title.

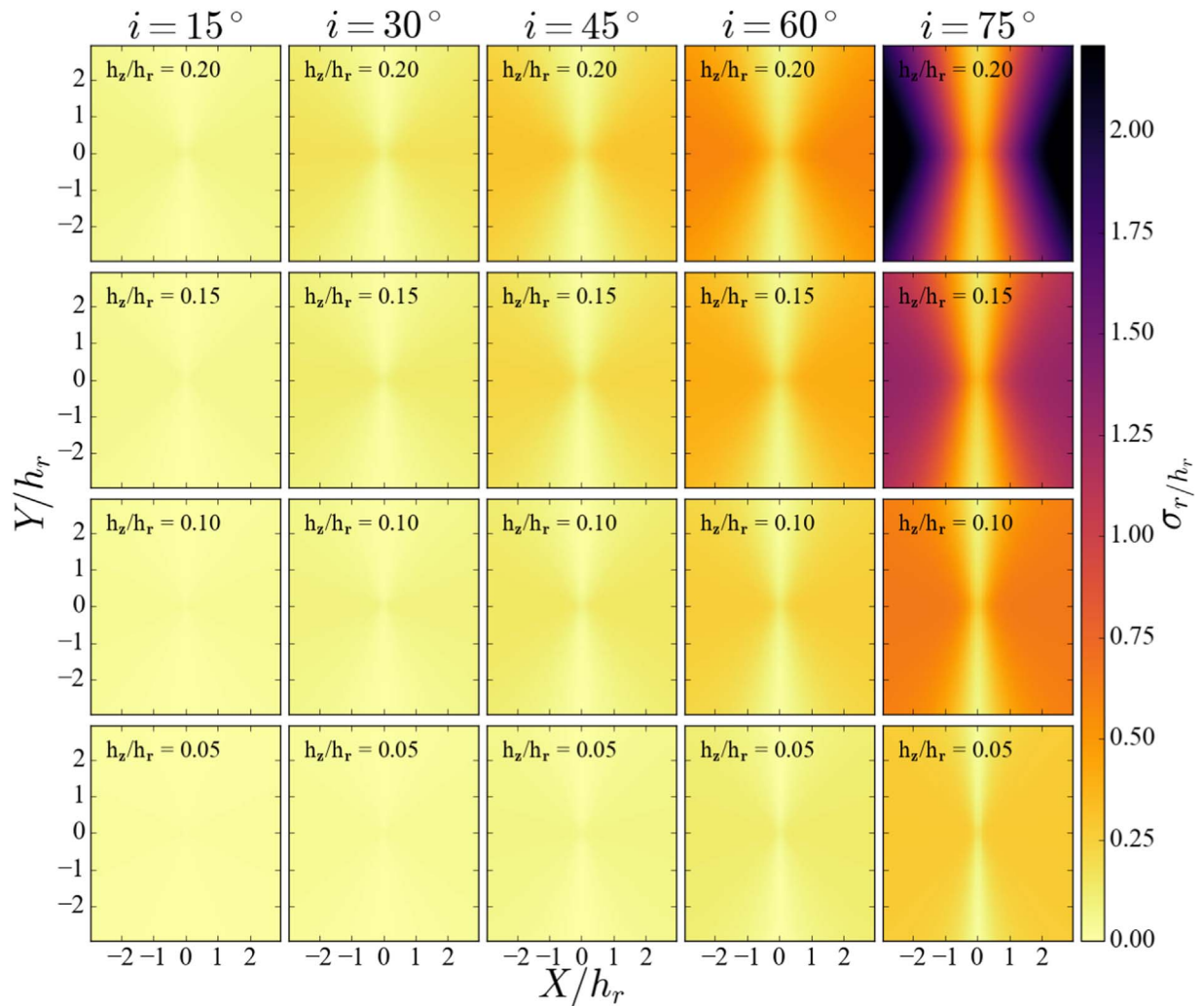


Figure 12. Maps of the dispersion in radius along the line of sight, in units of the radial exponential scale length. The apparent inclinations of the model disks increases from left to right ($i = 15^\circ, 30^\circ, 45^\circ, 60^\circ,$ and 75°), and the disk thickness increases from bottom to top ($h_z/h_r = 0.05, 0.1, 0.15,$ and 0.2). Away from the major axis, the range of radii probed increases with increasing inclination and disk thickness. This effect will tend to wash out gradients in the measured properties of stellar populations, unless confined to along the major axis.

effects would also produce significant scatter, as is evident in the PNe metallicity data for inner (< 15 kpc) disk PNe with low internal extinctions, thought to trace older populations mixed by M31’s recent merger (Bhattacharya et al. 2022).

In contrast to the PNe, H II regions do appear to show a modest radial metallicity gradient (e.g., Zurita & Bresolin 2012), which would be consistent with their being in a thinner gas disk with negligible projection effects. Alternatively, gas flows associated with a recent merger could potentially alter the distribution of current gas phase metallicities, while leaving the stellar metallicity distribution largely unaffected.

5.3. A Route to 3D Tomography

The calculation of the reddened fraction maps in Figure 3 implicitly assumes that the disk has a constant position and inclination angle, and that dust is in the midplane of the stellar disk, everywhere. These assumptions are likely to be sound for an undisturbed, well-settled galaxy. For galaxies with a more complicated recent interaction history, however, it is possible for there to be global warps that manifest in the maps of f_{red} , making the reddening maps a potentially powerful probe of the

3D galaxy structure. Indeed, this effect has already been demonstrated for the Large Magellanic Cloud, where Choi et al. (2018) has modeled observed reddening of red clump stars selected from the Survey of the Magellanic Stellar History (Nidever et al. 2017) and revealed the presence of a warp in the far outer stellar disk. Complementary work by Yanchulova Merica-Jones et al. (2021) in the Small Magellanic Cloud modeled the joint distribution of dust and stars from the red clump and RGB to infer the galaxy’s line-of-sight depth and offset between the gas and stellar midplane.

Empirically, warps are primarily phenomena of the outer disk. Stellar disk warps tend to emerge at $\sim R_{25}$ in edge-on late-type disks, and are typically modest ($\sim 1^\circ$ – 5° from the start of the warp; see Ann & Park 2006).¹⁶ In the inner regions, there is presumably enough stellar and dark matter mass to keep the different components coupled together (e.g., Ostriker & Binney 1989; Pranav & Jog 2010). In practice, examining warps in edge-on galaxies leads to observational biases that would suppress detection of deviations from a perfectly flat

¹⁶ For optically thin outer disks, the actual warp radius is likely to be beyond the face-on value of R_{25} , due to projection.

aligned disk in the inner disk, provided those deviations were modest and obscured by the dust lane. Indeed, low-amplitude warps or “waves” in the stellar disk have been revealed at the solar radius (and beyond) in the Milky Way (e.g., Widrow et al. 2012; Price-Whelan et al. 2015; Xu et al. 2015; Ferguson et al. 2017; Carrillo et al. 2018; Gaia Collaboration et al. 2018; Kawata et al. 2018; Schönrich & Dehnen 2018; Xiang et al. 2018; Ding et al. 2021; Gaia Collaboration et al. 2021; Ramos et al. 2021; Laporte et al. 2022) and numerical simulations (e.g., recently D’Onghia et al. 2016; Gómez et al. 2017; Chequers et al. 2018; Laporte et al. 2018; Gómez et al. 2020; Grión Filho et al. 2021; Hunt et al. 2021; Poggio et al. 2021).

Global warps can potentially be identified in reddening fraction maps. HI studies have long used changes in the position angle with the radius (via the kinematic line of nodes) to indicate the presence of warps (e.g., Briggs 1990). Similarly, one could use the locus of $f_{\text{red}} = 0.5$ to define the position angle as a function of the radius. Inspection of Figure 7 shows that $f_{\text{red}} = 0.5$ primarily along a single axis. However, there are also small deviations of the order of a degree or two in localized regions that could indicate warps. The amplitude of these position angle deviations are consistent with expectations from kinematical analysis of M31’s HI distribution (Chemin et al. 2009; Corbelli et al. 2010).

Additional features could be produced in reddening fraction maps if the gas layer that carries the dust becomes misaligned with respect to the bulk of the stars. These misalignments can be due to the differing dynamical responses of hot dissipationless (stellar) and cold dissipational (gaseous) disks, or due to different intrinsic angular momenta (say, if the gas had a different accretion origin).

Empirically, the gaseous and stellar disks appear to be globally well-aligned (to within a few percent) in the vast majority of edge-on galaxies, (see discussion in van der Kruit & Freeman 2011). This is not unexpected in general, given that if both the gas and stars are responding to a large-scale gravitational perturbation, then both will experience the same potential and maintain their relative alignment if given enough time to respond. However, in simulations such as Gómez et al. (2017) it is clear that there are small-scale vertical disturbances in the cold gas that are not reflected in the stellar disk (compare their Figures 2 and 4, for example), most likely because of the intrinsic difficulty in producing small-scale perturbations in high velocity dispersion dissipationless disks. Comparable gas deviations may have already been detected in the Milky Way (e.g., Levine et al. 2006) and in M31 in the early work by Braun (1991).

Small-scale gas-star deviations could also potentially be traced by the distribution of f_{red} . If the gas is pulled away from the midplane, the value of f_{red} at that location will shift. For example, Figure 7 shows a “spur” of gas at $\alpha \approx 11^\circ.3$, $\delta \approx 42^\circ.0$ with a uniform value of $f_{\text{red}} \approx 0.5$ over a larger range in azimuth than expected from the models in Figure 3. It is possible that this indicates a region where gas has been pulled away from the midplane. Similarly, accreted gas that has not yet settled to the midplane could also appear as a localized discrepancy in the reddening fraction.

In the future, it should be possible to create a full 3D tomographic model of M31 by combining the detailed structure of the reddening map with a Braun (1991)-style analysis of modern high-resolution HI data. Such a map could open up the

possibility of studying many effects of coupled gas and stellar dynamics in a system other than the Milky Way.

6. Conclusion

“Dust geometry” has long been a topic of interest, both for its impact on galaxies’ light distribution (e.g., Disney et al. 1989; Witt et al. 1992; Calzetti 2001) and for the study of the ISM itself (e.g., see the review by Galliano et al. 2018). This paper expands on the above work to highlight a less-widely appreciated role for measurements of dust geometry to be a potentially useful tool for understanding galaxy structure.

We have explained the optical morphology of M31 as being shaped by the combined structure of the stars and the dusty ISM. M31 shows a pronounced variation of the fraction of reddened RGB stars from one side of the major axis to the other. We measure this effect through modeling the NIR CMD, and find that on one side $\sim 80\%$ of stars along the line of sight are reddened, and on the other as few as $\sim 20\%$ of the stars are obscured by midplane dust. This variation can be straightforwardly explained by assuming that the path length through the stars is long enough to probe a large range of galactic radii. In this model, path lengths where the inner galaxy is on the near side of the dust will have more stars in front of the dust, and thus a low fraction of reddened stars.

We have interpreted the quantitative measurement of the reddening fraction by generating models of a thin dust layer embedded in a stellar disk with varying viewing angles and ratios of the radial to vertical exponential scale heights. By comparing the observed amplitude of the reddening variation and the observed axial ratio of M31 to these models, we constrain the old stellar disk of M31 to have $h_z/h_r = 0.14 \pm 0.015$. This axial ratio implies that the vertical exponential scale height is 770 ± 80 pc, for modern measurements of M31’s exponential disk at wavelengths dominated by RGB stars.

These measurements suggest that M31’s inferred scale height and disk axial ratio has far more in common with the Milky Way’s thick disk than its thin disk, in spite of being rather metal-rich ($[\text{Fe}/\text{H}] \gtrsim -0.2$; Gregersen et al. 2015; Escala et al. 2023). It is likewise unusually thick when compared to other edge-on galaxies.

While somewhat unusual, M31’s thickened disk is fully compatible with the evidence that M31 has experienced a rather major merger in the past 2–3 Gyr (see evidence compiled in Hammer et al. 2018 and D’Souza & Bell 2018b). Mergers have long been recognized as a means for vertically heating stellar disks (e.g., Quinn et al. 1993), and once a stellar disk is heated, it is typically unable to dynamically cool back into a colder, thinner disk. M31’s star formation rate is currently relatively low and typical of a “green valley” galaxy (Mutch et al. 2011), and as such has not had time to regrow a thinner disk of RGB stars. We suggest that M31’s morphology of highly asymmetric reddening can be used as a generic criterion for identifying comparable systems that are “thick disk” dominated.

We note that the large radial range probed within M31 is likely to impact measurements of radial gradients of stellar properties. In general, any metallicity and age gradients associated with >2 Gyr old populations will tend to be washed out by projection of multiple radii into a single projected position, making them appear to be weaker than they truly are. These effects are most significant away from the major axis,

and would be expected in any “puffy” disk viewed at moderate inclination.

In addition to providing knowledge about M31 itself, the work here reinforces some of the key points of Witt et al. (1992)’s *cri de couer*, most notably that the amount of reddening can be largely decoupled from the amount of dust. Both qualitatively and quantitatively, M31 shows a dramatic variation in the fraction of reddened stars, which obscures the large amount of dust on the southern half of the major axis. This single case offers a cautionary tale about the need to have a flexible treatment of dust geometry when modeling or interpreting spectra or photometry of resolved galaxies, particularly when those galaxies are inclined or warped.

Acknowledgments

The authors wish to thank Jo Bovy for providing an electronic version of the data used in Figure 10, and Bruce Elmegreen for pointing out his earlier work on explaining unusual reddening distributions. J.J.D. also thanks Adrian Price-Whelan, Vasily Belokurov, and Meredith Durbin for support and input in the final stages of this work. J.J.D. gratefully acknowledges the hospitality of the Max-Planck Institut für Astronomie during part of this work. This work was supported by the Space Telescope Science Institute through GO-12055. The Flatiron Institute is funded by the Simons Foundation. The authors made liberal use of Astropy, a community-developed core Python package for Astronomy (Astropy Collaboration et al. 2013), as well as numpy, scipy, and matplotlib (Hunter 2007; Oliphant 2007). This research has made use of NASA’s Astrophysics Data System Bibliographic Services and IPAC Science Archive.

Appendix

Calculating Polar Coordinates for an Inclined Disk

For the analysis in this paper, we map R.A. α and decl. δ into polar coordinates r and θ on the deprojected disk. We assume that the disk is centered at (α_0, δ_0) , and has an inclination i and a position angle ϕ . This disk will have an apparent axis ratio of $b/a = \cos i$ and eccentricity $\epsilon = \sqrt{1 - (b/a)^2}$. If we define angles relative to the center of disk (within a tangent plane) $\Delta\alpha = (\alpha - \alpha_0)\cos\delta_0$ and $\Delta\delta = \delta - \delta_0$, then the deprojected radius is

$$r^2 = (\Delta\delta \cos\phi + \Delta\alpha \sin\phi)^2 + \left[\frac{1}{\cos^2 i} \right] \times (\Delta\delta \sin\phi - \Delta\alpha \cos\phi)^2, \quad (\text{A1})$$

and the angular polar coordinate is

$$\cos\theta = \sqrt{1 - \left(\frac{y}{r}\right)^2}, \quad (\text{A2})$$

where

$$y = \Delta\delta \cos\phi + \Delta\alpha \sin\phi. \quad (\text{A3})$$

These relations hold for either an infinitely thin disk or the midplane of a thickened disk.

ORCID iDs

Julianne J. Dalcanton  <https://orcid.org/0000-0002-1264-2066>

Eric F. Bell  <https://orcid.org/0000-0002-5564-9873>

Yumi Choi  <https://orcid.org/0000-0003-1680-1884>
 Andrew E. Dolphin  <https://orcid.org/0000-0001-8416-4093>
 Morgan Fouesneau  <https://orcid.org/0000-0001-9256-5516>
 Léo Girardi  <https://orcid.org/0000-0002-6301-3269>
 David W. Hogg  <https://orcid.org/0000-0003-2866-9403>
 Anil C. Seth  <https://orcid.org/0000-0003-0248-5470>
 Benjamin F. Williams  <https://orcid.org/0000-0002-7502-0597>

References

- Ann, H. B., & Park, J.-C. 2006, *NewA*, 11, 293
 Astropy Collaboration, Robitaille, T. P., Tollerud, E. J., et al. 2013, *A&A*, 558, A33
 Athanassoula, E., & Beaton, R. L. 2006, *MNRAS*, 370, 1499
 Balick, B., Kwitter, K., & Corradi, R. 2017, in IAU Symp. 323, Planetary Nebulae: Multi-Wavelength Probes of Stellar and Galactic Evolution, ed. X. Liu, L. Stanghellini, & A. Karakas (Cambridge: Cambridge Univ. Press), 264
 Balick, B., Kwitter, K. B., Corradi, R. L. M., & Henry, R. B. C. 2013, *ApJ*, 774, 3
 Barmby, P., Ashby, M. L. N., Bianchi, L., et al. 2006, *ApJL*, 650, L45
 Beaton, R. L., Majewski, S. R., Guhathakurta, P., et al. 2007, *ApJL*, 658, L91
 Blańa Díaz, M., Wegg, C., Gerhard, O., et al. 2017, *MNRAS*, 466, 4279
 Blańa Díaz, M., Wegg, C., Gerhard, O., et al. 2017, *MNRAS*, 478, 611
 Beraldo e Silva, L., Debattista, V. P., Nidever, D., Amarante, J. A. S., & Garver, B. 2021, *MNRAS*, 502, 260
 Bernard, E. J., Ferguson, A. M. N., Richardson, J. C., et al. 2015, *MNRAS*, 446, 2789
 Bhattacharya, S., Arnaboldi, M., Caldwell, N., et al. 2019, *A&A*, 631, A56
 Bhattacharya, S., Arnaboldi, M., Caldwell, N., et al. 2022, *MNRAS*, 517, 2343
 Bizyaev, D. V., Kautsch, S. J., Mosenkov, A. V., et al. 2014, *ApJ*, 787, 24
 Blańa Díaz, M., Wegg, C., Gerhard, O., et al. 2017, *MNRAS*, 466, 4279
 Bland-Hawthorn, J., & Gerhard, O. 2016, *ARA&A*, 54, 529
 Bovy, J., & Rix, H.-W. 2013, *ApJ*, 779, 115
 Bovy, J., Rix, H.-W., & Hogg, D. W. 2012a, *ApJ*, 751, 131
 Bovy, J., Rix, H.-W., Liu, C., et al. 2012b, *ApJ*, 753, 148
 Braun, R. 1991, *ApJ*, 372, 54
 Briggs, F. H. 1990, *ApJ*, 352, 15
 Büdenbender, A., van de Ven, G., & Watkins, L. L. 2015, *MNRAS*, 452, 956
 Calzetti, D. 2001, *PASP*, 113, 1449
 Carrillo, I., Minchev, I., Kordopatis, G., et al. 2018, *MNRAS*, 475, 2679
 Chemin, L., Carignan, C., & Foster, T. 2009, *ApJ*, 705, 1395
 Chequers, M. H., Widrow, L. M., & Darling, K. 2018, *MNRAS*, 480, 4244
 Choi, P. I., Guhathakurta, P., & Johnston, K. V. 2002, *AJ*, 124, 310
 Choi, Y. 2016, PhD thesis, Univ. Washington (Seattle)
 Choi, Y., Nidever, D. L., Olsen, K., et al. 2018, *ApJ*, 866, 90
 Clark, C. J. R., Roman-Duval, J. C., Gordon, K. D., Bot, C., & Smith, M. W. L. 2021, *ApJ*, 921, 35
 Collins, M. L. M., Chapman, S. C., Ibata, R. A., et al. 2011, *MNRAS*, 413, 1548
 Comerón, S., Elmegreen, B. G., Knapen, J. H., et al. 2011, *ApJ*, 741, 28
 Corbelli, E., Lorenzoni, S., Waltherbos, R., Braun, R., & Thilker, D. 2010, *A&A*, 511, A89
 Courteau, S., Widrow, L. M., McDonald, M., et al. 2011, *ApJ*, 739, 20
 Crnojević, D., Sand, D. J., Spekkens, K., et al. 2016, *ApJ*, 823, 19
 Dalcanton, J. J., & Bernstein, R. A. 2002, *AJ*, 124, 1328
 Dalcanton, J. J., Fouesneau, M., Hogg, D. W., et al. 2015, *ApJ*, 814, 3
 Dalcanton, J. J., Williams, B. F., Lang, D., et al. 2012, *ApJS*, 200, 18
 Deason, A. J., Belokurov, V., Koposov, S. E., & Lancaster, L. 2018, *ApJL*, 862, L1
 Ding, P.-J., Xue, X.-X., Yang, C., et al. 2021, *AJ*, 162, 112
 Disney, M., Davies, J., & Phillipps, S. 1989, *MNRAS*, 239, 939
 D’Onghia, E., Madau, P., Vera-Ciro, C., Quillen, A., & Hernquist, L. 2016, *ApJ*, 823, 4
 Dorman, C. E., Guhathakurta, P., Fardal, M. A., et al. 2012, *ApJ*, 752, 147
 Dorman, C. E., Guhathakurta, P., Seth, A. C., et al. 2015, *ApJ*, 803, 24
 Dorman, C. E., Widrow, L. M., Guhathakurta, P., et al. 2013, *ApJ*, 779, 103
 Draine, B. T., Aniano, G., Krause, O., et al. 2014, *ApJ*, 780, 172
 D’Souza, R., & Bell, E. F. 2018a, *MNRAS*, 474, 5300
 D’Souza, R., & Bell, E. F. 2018b, *NatAs*, 2, 737
 Elmegreen, B. G., & Block, D. L. 1999, *MNRAS*, 303, 133
 Elmegreen, B. G., Elmegreen, D. M., Tompkins, B., & Jenks, L. G. 2017, *ApJ*, 847, 14

- Escala, I., Quirk, A. C. N., Guhathakurta, P., et al. 2023, *AJ*, 165, 75
- Ferguson, D., Gardner, S., & Yanny, B. 2017, *ApJ*, 843, 141
- Foreman-Mackey, D., Hogg, D. W., Lang, D., & Goodman, J. 2013, *PASP*, 125, 306
- Fritz, J., Gentile, G., Smith, M. W. L., et al. 2012, *A&A*, 546, A34
- Gaia Collaboration, Antoja, T., McMillan, P. J., et al. 2021, *A&A*, 649, A8
- Gaia Collaboration, Katz, D., Antoja, T., et al. 2018, *A&A*, 616, A11
- Gajda, G., Gerhard, O., Blaňa, M., et al. 2021, *A&A*, 647, A131
- Galliano, F., Galametz, M., & Jones, A. P. 2018, *ARA&A*, 56, 673
- Gilbert, K. M., Quirk, A. C. N., Guhathakurta, P., et al. 2022, *ApJ*, 924, 116
- Gómez, F. A., Torres-Flores, S., Mora-Urrejola, C., et al. 2020, arXiv:2011.12323
- Gómez, F. A., White, S. D. M., Grand, R. J. J., et al. 2017, *MNRAS*, 465, 3446
- Hegresen, D., Seth, A. C., Williams, B. F., et al. 2015, *AJ*, 150, 189
- Greggio, L., Rejkuba, M., Gonzalez, O. A., et al. 2014, *A&A*, 562, A73
- Grion Filho, D., Johnston, K. V., Poggio, E., et al. 2021, *MNRAS*, 507, 2825
- Hammer, F., Yang, Y. B., Wang, J. L., et al. 2018, *MNRAS*, 475, 2754
- Harmesen, B., Monachesi, A., Bell, E. F., et al. 2017, *MNRAS*, 466, 1491
- Haywood, M., Di Matteo, P., Lehnert, M. D., et al. 2018, *ApJ*, 863, 113
- Helmi, A. 2020, *ARA&A*, 58, 205
- Helmi, A., Babusiaux, C., Koppelman, H. H., et al. 2018, *Natur*, 563, 85
- Keyer, M., & Dame, T. M. 2015, *ARA&A*, 53, 583
- Holwerda, B. W., Dalcanton, J. J., Radburn-Smith, D., et al. 2012, *ApJ*, 753, 25
- Hawk, J. C., & Savage, B. D. 1999, *AJ*, 117, 2077
- Hunt, J. A. S., Stelea, I. A., Johnston, K. V., et al. 2021, *MNRAS*, 508, 1459
- Hunter, J. D. 2007, *CSE*, 9, 90
- Ibata, R., Chapman, S., Ferguson, A. M. N., et al. 2005, *ApJ*, 634, 287
- Ibata, R. A., Lewis, G. F., McConnachie, A. W., et al. 2014, *ApJ*, 780, 128
- Jacoby, G. H., & Ciardullo, R. 1999, *ApJ*, 515, 169
- Jurić, M., Ivezić, Ž., Brooks, A., et al. 2008, *ApJ*, 673, 864
- Karachentsev, I. D., Karachentseva, V. E., & Parnovskij, S. L. 1993, *AN*, 314, 97
- Kawata, D., Baba, J., Ciucă, I., et al. 2018, *MNRAS*, 479, L108
- Kwitter, K. B., Lehman, E. M. M., Balick, B., & Henry, R. B. C. 2012, *ApJ*, 753, 12
- Laporte, C. F. P., Johnston, K. V., Gómez, F. A., Garavito-Camargo, N., & Besla, G. 2018, *MNRAS*, 481, 286
- Laporte, C. F. P., Kopusov, S. E., & Belokurov, V. 2022, *MNRAS*, 510, L13
- Levine, E. S., Blitz, L., & Heiles, C. 2006, *ApJ*, 643, 881
- Marasco, A., Fraternali, F., van der Hulst, J. M., & Oosterloo, T. 2017, *A&A*, 607, A106
- Mateu, C., & Vivas, A. K. 2018, *MNRAS*, 479, 211
- Merrett, H. R., Merrifield, M. R., Douglas, N. G., et al. 2006, *MNRAS*, 369, 120
- Merritt, A., van Dokkum, P., Abraham, R., & Zhang, J. 2016, *ApJ*, 830, 62
- Mosenkov, A. V., Sotnikova, N. Y., Reshetnikov, V. P., Bizyaev, D. V., & Kautsch, S. J. 2015, *MNRAS*, 451, 2376
- Mouhcine, M., Ibata, R., & Rejkuba, M. 2010, *ApJL*, 714, L12
- Mutch, S. J., Croton, D. J., & Poole, G. B. 2011, *ApJ*, 736, 84
- Nidever, D. L., Olsen, K., Walker, A. R., et al. 2017, *AJ*, 154, 199
- Oliphant, T. E. 2007, *CSE*, 9, 10
- Opitsch, M., Fabricius, M. H., Saglia, R. P., et al. 2018, *A&A*, 611, A38
- Ostriker, E. C., & Binney, J. J. 1989, *MNRAS*, 237, 785
- Poggio, E., Laporte, C. F. P., Johnston, K. V., et al. 2021, *MNRAS*, 508, 541
- Pranav, P., & Jog, C. J. 2010, *MNRAS*, 406, 576
- Price-Whelan, A. M., Johnston, K. V., Sheffield, A. A., Laporte, C. F. P., & Sesar, B. 2015, *MNRAS*, 452, 676
- Quinn, P. J., Hernquist, L., & Fullagar, D. P. 1993, *ApJ*, 403, 74
- Ramos, P., Antoja, T., Mateu, C., et al. 2021, *A&A*, 646, A99
- Rejkuba, M., Harris, W. E., Greggio, L., et al. 2014, *ApJL*, 791, L2
- Rueff, K. M., Howk, J. C., Pitterle, M., et al. 2013, *AJ*, 145, 62
- Sanders, N. E., Caldwell, N., McDowell, J., & Harding, P. 2012, *ApJ*, 758, 133
- Schönrich, R., & Dehnen, W. 2018, *MNRAS*, 478, 3809
- Seigar, M. S., Barth, A. J., & Bullock, J. S. 2008, *MNRAS*, 389, 1911
- Sharma, S., Hayden, M. R., Bland-Hawthorn, J., et al. 2021, *MNRAS*, 506, 1761
- Toth, G., & Ostriker, J. P. 1992, *ApJ*, 389, 5
- Trujillo, I., & Fliri, J. 2016, *ApJ*, 823, 123
- van der Kruit, P. C., & Freeman, K. C. 2011, *ARA&A*, 49, 301
- Widrow, L. M., Gardner, S., Yanny, B., Dodelson, S., & Chen, H.-Y. 2012, *ApJL*, 750, L41
- Wild, V., Charlot, S., Brinchmann, J., et al. 2011, *MNRAS*, 417, 1760
- Williams, B. F., Dalcanton, J. J., Dolphin, A. E., et al. 2015, *ApJ*, 806, 48
- Williams, B. F., Dolphin, A. E., Dalcanton, J. J., et al. 2017, *ApJ*, 846, 145
- Williams, B. F., Lang, D., Dalcanton, J. J., et al. 2014, *ApJS*, 215, 9
- Witt, A. N., Thronson, H. A. J., & Capuano, J. M. J. 1992, *ApJ*, 393, 611
- Wu, Y., Xiang, M., Chen, Y., et al. 2021, *MNRAS*, 501, 4917
- Xiang, M., Shi, J., Liu, X., et al. 2018, *ApJS*, 237, 33
- Xilouris, E. M., Byun, Y. I., Kylafis, N. D., Paleologou, E. V., & Papamastorakis, J. 1999, *A&A*, 344, 868
- Xu, Y., Newberg, H. J., Carlin, J. L., et al. 2015, *ApJ*, 801, 105
- Yanchulova Merica-Jones, P., Sandstrom, K. M., Johnson, L. C., et al. 2021, *ApJ*, 907, 50
- Yoachim, P., & Dalcanton, J. J. 2006, *AJ*, 131, 226
- Yoachim, P., & Dalcanton, J. J. 2008, *ApJ*, 682, 1004
- Zurita, A., & Bresolin, F. 2012, *MNRAS*, 427, 1463